Materials and Design 166 (2019) 107618

Contents lists available at ScienceDirect

Materials and Design

journal homepage: www.elsevier.com/locate/matdes

# A metallurgical phase transformation framework applied to SLM additive manufacturing processes

Qi Zhang [c,a,*], Jiawen Xie [a], Zhenyuan Gao [d], Tyler London [b], David Griffiths [b], Victor Oancea [a]

[a] Dassault Systemes SIMULIA Corp., Johnston, RI, USA
[b] TWI Ltd, Cambridge, UK
[c] Brown University, Providence, RI, USA
[d] Purdue University, West Lafayette, IN, USA

## HIGHLIGHTS

- A generic framework for simulation of Additive Manufactured parts
- Linking thermal model to microstructural features
- Model validation in Ti-6Al-4 V and Steel 5140
- Experiments and simulations of Selective Laser Melting processed Ti-6Al-4 V samples
- Microstructure assessment of as-built and heat-treated Ti-6Al-4 V samples

## GRAPHICAL ABSTRACT

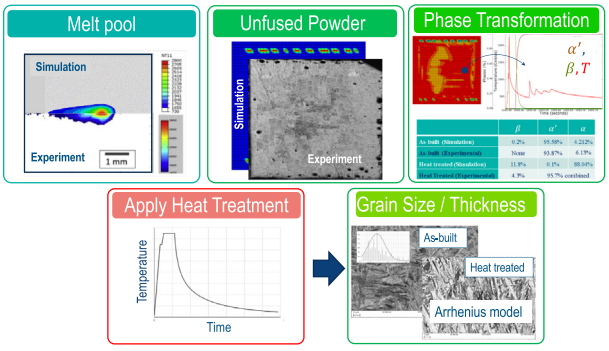


## ARTICLE INFO

*Article history:*
Received 15 October 2018
Received in revised form 20 December 2018
Accepted 24 January 2019
Available online 26 January 2019

*Keywords:*
AM process simulation
Powder bed fabrication
Thermal-stress analysis
Microstructure
Finite elements
Selective laser melting

## ABSTRACT

While significant progress has been made in the last few years, the reliability of Additively Manufactured (AM) parts is often less than desirable as they suffer from manufacturing defects and hence subpar strength and fatigue life. To address this challenge, numerical methods are sought to provide insight into the process and help accelerate progress in raising the quality of AM parts. In metal AM applications, assessing the amount of unfused powder, melt pool volumes, and metallurgical phase transformations is often of interest. In this work, we introduce a generic framework for assessing metallurgical phase transformations, building on a previously-developed general simulation framework for predicting temperature evolution, distortions, and residual stresses. Experimental work was conducted to validate numerical predictions and included temperature measurements, EBSD/XRD microstructural examinations. Additional test data from the published literature was used to validate melt pool sizes and unfused powder predictions. We conclude that the continuum-level internal state variable approach proposed here can be calibrated with a reasonable amount of effort and can be used directly to link processing conditions to microstructural features. Upcoming work investigates the influence of microstructure features on mechanical performance to address the process-structure-property-performance relationship in SLM additive manufacturing.


## 1. Introduction

In previous work [1], a customizable general simulation framework has been demonstrated and validated for a wide spectrum of additive

* Corresponding author.
*E-mail address:* qi_zhang@alumni.brown.edu (Q. Zhang).

https://doi.org/10.1016/j.matdes.2019.107618

manufacturing (AM) processes (laser and electron beam powder bed fabrication, direct energy deposition, arc welding, polymer extrusion, ink jetting) as implemented on the Dassault Systèmes 3DX Platform based on new Finite Element (FE) technology implemented in Abaqus. The framework allows for: 1) arbitrary meshes of CAD representations; 2) exact specification in time and space of processing conditions (e.g., powder addition, laser trajectories, dwell times, etc.); 3) precise tracking of the progressive addition of raw material to each element in the mesh via complex geometric computations; 4) precise integration of the moving energy sources (e.g., laser, electron beams, arc welds, high temperature polymer extrusion) and; 5) automatic computation of the continuously evolving convection and radiation surfaces.

In the current work, in conjunction with the general simulation framework above, a generic metallurgical phase transformation framework applicable to arbitrary metal alloys is introduced. The framework accounts for phase transformations (physical state changes) from stock feed or raw material (e.g., powder) via melting/vaporization/solidification followed by metallurgical solid-state phase transformations induced by either rapid heating or cooling events associated with typical 3D printing sequences but also with slower-rate temperature evolutions as associated with heat treatment applications [2]. The user systematically defines all possible transformations that can take place via a parent-children paradigm (e.g., austenite to martensite); the temperature conditions when transformations can occur with associated time-temperature-transformation (TTT) diagrams; and whether the transformations are reversible, diffusional, or non-diffusional. The framework predicts temperature evolutions, calibrates models of transformation kinetics, and predicts phase transformations during printing and heat treatment. Grain growth and grain aspect ratio assessment models are also implemented. At this time, the framework does not account for precipitate formation (e.g., Anderson [3]).

Experimental work is always necessary in order to gain insight into the physics governing the processes being studied. Since numerical models are only valuable if they are reasonably predictive, a number of targeted experiments were conducted with the dual scope of understanding solidification behavior and to verify and validate the numerical predictions. In addition to previous work of the authors [1], a number of validation exercises relying on a minimal amount of calibration activity were performed in this work. First, the overall thermal balance of the printing process was studied by recording the temperature evolutions at thermocouples placed in the build plate while the printing process is ongoing. Second, melt pool size assessments against physical tests were executed. After gaining confidence that the thermal evolutions (heating and cooling rates and thermal gradients) were predicted with reasonable accuracy, a third round of experiments were conducted to measure via SEM, EBSD and XRD techniques the post-printing and post-heat treatment the volume fraction of phases present as well as thickness of the lamellar structures developed.

The paper is organized as follows. In Section 2, a brief review of the general FE-based framework utilized for thermo-mechanical analysis of the printing process is performed. In Section 3, the generic metallurgical phase transformation model for any alloy is presented. Two detailed exemplifications are given in Section 4, for Ti-6Al-4V and steel 5140. Finally, in Section 6, conclusions are drawn to outline the success but also the remaining challenges.

## 2. Finite element simulation of powder-bed fusion additive manufacturing

New physics-based FEM formulations and models implemented in software Apps from DASSAULT SYSTEMES R2018x [4] were used in this study. It is not the focus of this paper to describe these features in detail, but key aspects of the framework include:

- Meshing: the geometric shape of the part whose 3D printing process is to be modeled is first discretized with finite elements. Arbitrary mesh densities can be used as generated by existing pre-processors. This overcomes the challenge of producing uniform, voxel-based or layer-conforming finite element meshes which are difficult, if not impractical, to generate for complex, topology optimized geometries that are often of interest to manufacture using powder-bed fusion processes.
- Machine information: the 3D printing machine related information (e.g., powder recoating sequence, laser scan path, material deposition of the printing head, arc weld power, etc.) is pre-processed with no loss of accuracy from actual data as used by the physical machines.
- A path intersection module: the path intersection algorithm is used to sweep through the finite element mesh with the laser scanning sequence (or tool path) and associated heat source configurations. The intersection can be based on either the original shape of the part or the current shape of the predicted deformed/distorted shape of the part during the analysis.
- Progressive element activation: at any given point during the simulation, any finite element could be completely filled with matter, partially filled with matter, or completely empty. The calculation method precisely keeps track of this evolution, keeps track of the mass inventory and distribution to account for the addition of the material during the printing. This is a significant step-change in AM process simulation technology from conventional element birth techniques.
- Progressive heating computations: at any point in time, heat bursts are computed by taking into account the actual path and power distribution of the heat source (the laser beam in this case). An arbitrary number of heating events (characterized as a sequence of heat fluxes at given locations) are computed for an accurate representation of the heating source in both time and space.
- Progressive cooling via convection and radiation: partial facet areas are computed to allow for a precise assessment of cooling-related heat fluxes, regardless of the finite element discretization. Radiation and convective heat transfer can be modeled on a continuously evolving surface that reflects the current shape of the part at any given point during the print. As indicated previously, this represents a step-change over confirming element activation methods.
- Openness: a comprehensive set of new APIs are available to access information computed inside the code. While solutions for all major AM processes are provided, users can tailor physics modeling needs corresponding the particular process, machine environment, etc.

### 2.1. Overall modeling considerations

The Apps are based on the FE solver Abaqus and the usual transient heat transfer and quasi-static stress divergence balance equations are leveraged. For brevity they will not be reviewed here but the details are outlined in the software's User Manuals [4].

In this study, the laser heat source is considered as a distributed volumetric heat flux and modeled by Goldak's semi-ellipsoid model [5]. In the local $x$-$y$-$z$ frame of the laser, where $x$-axis aligns with the direction of travel, the laser heat source is described as

$$Q(x,y,z,t) = \frac{2P\eta}{\bar{a}\bar{b}\bar{c}\pi\sqrt{\pi}} \exp\left[-\left(\frac{(x+v_x t)^2}{\bar{a}^2} + \frac{(y)^2}{\bar{b}^2} + \frac{(z)^2}{\bar{c}^2}\right)\right] \quad (1)$$

where $P$ is the nominal power, $\eta$ is absorption coefficient and $v_x$ is the travel speed of the laser; $t$ is the time; and $\bar{a}$, $\bar{b}$, and $\bar{c}$ are the dimensions of the ellipsoid along $x$-, $y$- and $z$-axis, respectively. The dimensions can be defined by laser parameters, including radius $r$, eccentricity $e$ and penetration depth $d$, as $\bar{a} = er, \bar{b} = \frac{r}{e}, \bar{c} = d$.

Thermal radiation $q_{rad} = \varepsilon\sigma((T - T_z)^4 - (T_\infty - T_z)^4)$, and surface convection $q_{conv} = h(T - T_\infty)$ of free surfaces during manufacturing processes are considered, where $T$ is the temperature, $\varepsilon$ is the material

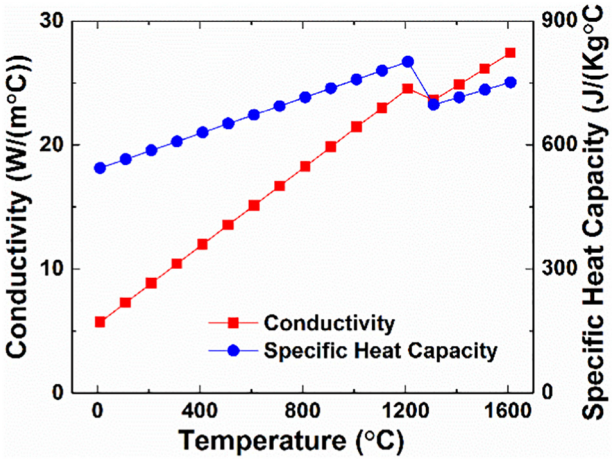


**Fig. 1.** Ti-6Al-4V thermal properties: conductivity and specific heat capacity.

emissivity, $h$ is convective coefficient, $\sigma = 5.67 \times 10^{-8}$ W/(m$^2 \cdot {}^\circ$C$^4$) is the Stefan-Boltzmann constant, $T_z = -273.15^\circ$C is the absolute zero temperature, and $T_\infty$ is the ambient temperature.

For the stress analysis, the temperatures are read from the heat transfer analysis. Similar techniques as described above are used to add material during the stress analysis.

As for the material properties, temperature-dependent material models for conductivity, specific heat, latent heat for melting and vaporization [6] were chosen as shown in Fig. 1, Tables 1 and 2.

### 2.2. AM predictive simulations: Spatial and time multiscale considerations

The gigantic multiscale problem in both space and time associated with additive manufacturing process simulation has been well discussed in the literature [7,8]. The multi-physics relevant for sub-millimeter melt pools combined with local cooling rates of thousands of degrees Celsius per second contrast with the typical dimensions of parts being printed accompanied with printing times of hours/days.

When it comes to predicting far field temperature evolutions (away from the areas where active melting/fusion occurs) during print and post removal from build plate distortions, averaged/lumped techniques in meshes and time increments can be employed with reasonable reliability [1]. In addition to the averaged techniques, macroscale phenomenological temperature-dependent elasto-plastic constitutive models appear to be reliable and computationally efficient for effective simulations when it comes to predicting the distortions and stresses in printed metal parts.

However, in order to capture the rapidly evolving temperature evolutions and high temperature gradients associated with the melt pools and their vicinity, special care must be exercised for both the meshes being used as well as the time marching strategies.

A coarse mesh is employed in regions away from the zone of interest while a fine mesh with a 20 μm characteristic dimension is used in the areas where metallurgical phase transformations computations are performed. After a mesh convergence study, it was found that this is the coarsest mesh (and hence most economical) that allows for accurate computation of thermal gradients. In addition, a coarse time stepping scheme is adopted in regions away from the zone of interest or for most of the time associated with the recoating process when temperature evolution rates are low. By contrast, the time stepping in the regions of interest during laser scanning is adopted to be close to 1 ms. After a time stepping convergence study, it was found that this is the coarsest time step that allows for accurate computation of heating and cooling rates associated with the vicinity of the melt pools.

**Table 1**
Latent heat of Ti-6Al-4V.

| | |
|---|---|
| Latent heat of fusion | **2.86 × 10$^5$ J/kg** |
| Solidus temperature | 1604°C |
| Liquidus temperature | 1650°C |
| Latent heat of vaporization | 9.83 × 10$^6$ J/kg |
| Liquidus temperature | 3290°C |
| Vaporized temperature | 3390°C |

**Table 2**
Other thermal properties of Ti-6Al-4V.

| | |
|---|---|
| Density $\rho$ | **4420 kg/m$^3$** |
| Emissivity $\epsilon$ | 0.25 |
| Convection Coefficient $h$ | 18 W/(m$^2 \cdot$ °C) |

While the framework was able to predict well the size of the melt pools in the areas where a fine finite element mesh is employed, the model accounts only phenomenologically for the very complex physics inside the melt pool. The thermal conductivity of the powder was taken to be 10 times lower than the thermal conductivity of the solidified material but there are no CFD computations and Marangoni-driven convection patterns inside the pool. Instead the parameters of the Goldak heating model were calibrated such that the melt pool size matched experimental values.

The finer finite element meshes were numerically "glued" to the coarser meshes used in the other areas and therefore the heat gets transferred to these other areas via these interfaces [9]. Importantly, the path intersection module described above [4,9] allows for a wide range of ratios of element sizes when compared to the Goldak semi-ellipsoidal characteristic dimensions. Only in the areas where the fine meshes were employed (several elements in the melt pool) the model is able to capture the non-uniform energy density distribution. In the areas of coarser meshes, the model is largely equivalent with a concentrated moving point heat flux.

## 3. An FE-based generic metallurgical phase transformation framework

Previous work of the authors [1] implemented a phenomenological metallurgical phase transformation model for Ti-6Al-4V alloy [10] within the general simulation framework of additive manufacturing processes, and validated the predicted porosity (unfused areas) and phase content against experiment measurements. In this paper, the model for Ti-6Al-4V is extended to a generic framework applicable to arbitrary metal alloys.

First, the framework considers physical state changes from a stock feed (i.e. a raw material, such as a powder) via melting, vaporization, and solidification. During an additive manufacturing process, raw (unfused) materials are melted to a liquid state by an intense moving heat source, and then undergoes cooling and solidification when the heat source is removed. The solidified (fused) material can be re-melting when the heat source passes by a nearby location. As shown in Fig. 2, transitions between raw, liquid, and solid states of an alloy

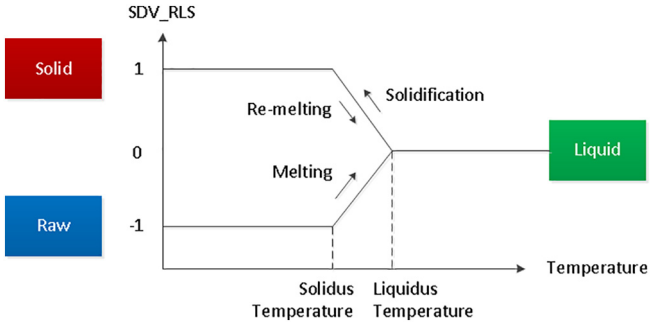


**Fig. 2.** Diagram of physical state changes between raw/liquid/solid (RLS) states.

material are considered as govern simply by temperature and occurring in a temperature range bounded by the solidus and liquidus temperature of the alloy. Thus, melt pool size and unfused zones can be predicted. Thermal and mechanical properties as a function of the physical state of the materials can also be considered in FE simulations. It should be noted that this method does not consider porosity that might arise due to melt pool turbulence and the entrapment (or release) of gases during processing. To approximate such phenomena, semi-empirical models have been used for casting simulations [11,12] or computational fluid dynamics studies for laser welding (with applicability to laser-based AM) [13] have previously been used.

Secondly, the framework accounts for metallurgical solid-state phase transformations induced by heating and cooling events associated with rapid manufacturing processes and/or slower heat treatment applications. Modeling of metallurgical solid phase transformations is discussed below. The onset and the speed of transformations are associated with the alloy's TTT diagram that can be measured experimentally or generated by commercial software such as JMatPro and ThermoCalc. As a result, distribution and evolutions of the solid-phase composition that further influences thermal and mechanical behavior can be assessed. The framework is based on phenomenological (internal state variable) metallurgical phase transformation models and, therefore, it is not a replacement for JMatPro or ThermoCalc or discrete-level methods.

### 3.1. Kinetics of solid-phase transformations

A solid-phase transformation can be written in a form of

$$p_1 + p_2 + \ldots + p_{n_p} \rightarrow c_1 + c_2 + \ldots + c_{n_c} \tag{2}$$

where $n_p$ and $n_c$ are numbers of the parent and children phases, respectively; $p_i$ and $c_i$ denote the $i$th parent phase, and the $i$th child phases, respectively. The change of volume fraction of a parent phase during a transformation is assumed to be proportional to its current volume fraction. A similar assumption is made for children phases. With these assumptions, a transformation can be simplified as $p \rightarrow c$. It consists of one master parent phase and one master child phase. The volume fractions of the master phases are $f_p = \sum_{i=1}^{n_p} f_{p_i}$ and $f_c = \sum_{i=1}^{n_c} f_{c_i}$, respectively. Two types of transformations are considered, diffusional transformation and martensitic (non-diffusional) transformation.

The kinetics of a diffusional transformation under isothermal conditions can be described by the Johnson-Mehl-Avrami (JMA) model [10].

$$f_c = f_{tot}(1 - \exp[-kt^n]) \tag{3}$$

where $f_{tot} = f_p + f_c$ is the total volume fraction of all parent and children phases participated in the transformation; $k$ and $n$ are temperature-dependent coefficients that can be calibrated from TTT diagrams. Fig. 3 shows an example TTT diagram that plots a diffusional transformation (D) and a martensitic transformation (M). A transformation is usually represented by at least two curves in a TTT diagram: a start curve (e.g., $D_s$, $M_s$ in Fig. 3) that marks the beginning of the transformation and a finish curve (e.g., $D_f$, $M_f$ in Fig. 3) where the transformation is completed. A curve in a TTT diagram represents the time (as a function of temperature) that a transformation has completed a certain percentage. For instance, the start curve of the diffusional transformation $D_s$ can be represented by the time, $t_s^D(T)$, when the transformation begins and the corresponding volume fraction of the children phases, $f_s^D$. Thus, the JMA coefficients of a diffusional transformation can be calibrated from TTT curves as $n(T) = \frac{\log[\log(1-f_s^D)/\log(1-f_f^D)]}{\log[t_s^D(T)/t_f^D(T)]}$ and $k(T) = -\frac{\log(1-f_s^D)}{(t_s^D(T))^{n(T)}}$.

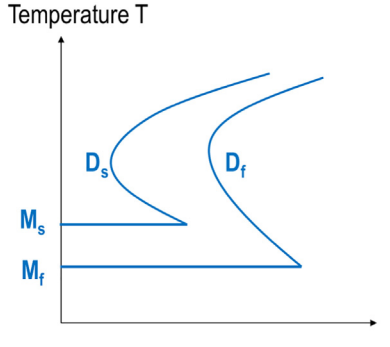


**Fig. 3.** An example time-temperature-transformation (TTT) diagram.

Additive manufacturing processes involve rapid heating and cooling events that are considered as non-isothermal conditions. Therefore, an extended JMA model [10] that considers continuous temperature variation as a series of small consecutive isothermal steps is used

$$f_p(T + \Delta T) = f_{tot}\left(1 - \left(1 - \exp\left[-k(\xi + \Delta t)^n\right]\right)\left(1 - f_{p,0}^{eq}\right)\right), \quad \text{if } f_p > f_{tot} f_{p,0}^{eq} \tag{4}$$

where $\Delta t$ is the time step size; $\Delta T$ is the temperature change since the last step; $f_{p,0}^{eq}$ are temperature-dependent equilibrium volume fractions of all parent phases in the mixture that only contains parent and children phases of the transformation; $\xi$ is the fictitious time which would provide the same amount of transformation, resulted in volume fraction, $f_p(T)$, at a constant temperature $T + \Delta T$, defined as $\xi = \left[-\frac{1}{k}\ln\left(\frac{f_p(T) - f_{tot} f_{p,0}^{eq}}{f_{tot}(1 - f_{p,0}^{eq})}\right)\right]^{\frac{1}{n}}$.

If the diffusional transformation is reversible ($p \leftrightarrow c$), the reverse transformation $c \rightarrow p$ can be described as

$$f_p(T + \Delta T) = f_{tot}\left(1 - \exp\left[-k(\xi + \Delta t)^n\right]\right) f_{p,0}^{eq}, \quad \text{if } f_p < f_{tot} f_{p,0}^{eq} \tag{5}$$

Above all, the logic to model a diffusional transformation is summarized in Fig. 4.

A martensitic transformation solely depends on temperature, as described by the Koistinen-Marburger (KM) model [10],

$$f_c(T) = f_c(T_o) + \left(f_p(T_o) - f_{pr}\right)[1 - \exp[-\gamma(M_s - T)] \tag{6}$$

where $T_o$ is the temperature at the beginning of the current cooling cycle; the martensitic start temperature $M_s$ and the transformation coefficient $\gamma$ can be calibrated from TTT diagrams. Since a martensitic transformation is independent of time, this type of transformation is usually represented by at least two horizontal lines in the TTT diagram, as shown in Fig. 3. For example, the start curve of the martensitic transformation can be represented by the temperature $M_s$ where the transformation begins and the corresponding volume fraction of the children phases $f_s^M$. Thus, the transformation coefficient $\gamma$ can be computed as $\gamma = -\frac{\log[(1-f_s^M)/(1-f_f^M)]}{M_f - M_s}$.

Under arbitrary thermal histories, a backward Euler integration of the differential form of the original KM model [1] is used

$$f_c(T + \Delta T) = \frac{f_c(T) - \gamma \Delta T\left(f_p(T_0) - f_{p_r} + f_p(T_0)\right)}{1 - \gamma dT} \tag{7}$$

The transformation occurs if the initial volume fraction of parent phases is higher than the retained amount of parent phases, namely, $f_p(T_0) > f_{p_r}$. The algorithm to model a martensitic transformation is shown in Fig. 5.

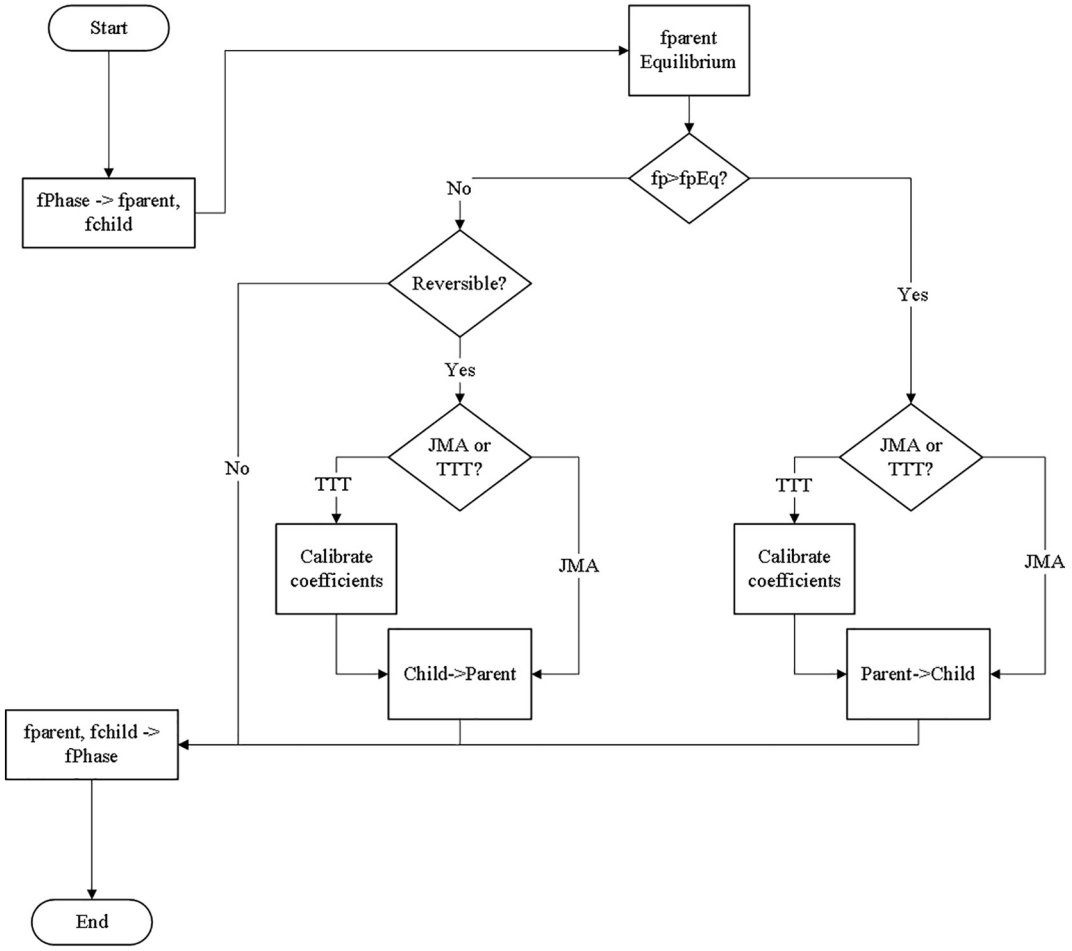


**Fig. 4.** The algorithm to model a diffusional transformation.

After the volume fraction of the master phases of a transformation are computed, the volume fraction of parent and children phases can be updated as $f_{p_i}(T+\Delta T) = f_p(T+\Delta T)\frac{f_{p_i}(T)}{f_p(T)}$, $f_{c_i}(T+\Delta T) = f_c(T+\Delta T)\frac{f_{c_i}(T)}{f_c(T)}$.

### 3.2. Modeling framework

The generic metallurgical phase transformation framework is implemented via user subroutine USDFLD that can be called by FE solver Abaqus/Standard at each integration point in each increment during simulations. Results, including physical state of the material and volume fractions of solid phases, are stored as field variables for visualization and can be further used to evaluate thermal and mechanical properties as a function of those quantities. In each increment, the physical state of the material is first assessed. If the material is in the solid state, metallurgical phase transformations are evaluated by following the general algorithm shown in Fig. 6. The computation loops over all possible solid-phase transformations. The transformations satisfying the condition of temperature and/or temperature rate for occurring are computed and the volume fractions of its parent and children phases are updated. Two types of transformations, diffusional and martensitic transformation, are modeled in separate subroutines. In this framework, one can model any number of phases and transformations as desired. Priority of transformations is considered as the same as the input sequence of transformations if any two transformations can be concurrent. Future work will include considerations of the coupling of concurrent transformations.

The framework allows the user to systematically define and to model phase transformations in an alloy during arbitrary additive manufacturing process. Modeling parameters are associated with the alloy's phase diagram and TTT diagram, including solidus and liquidus temperature, numbers and names of solid phases and solid-phase transformations, phase fraction upon solidification; and for each transformation, numbers and names of parent and children phases, the transformation type, reversibility, temperature conditions when transformations can occur, curves in TTT diagrams for calibrating the JMA and KM models or calibrated model coefficients, etc. Together with the general simulation framework of additive manufacturing processes, the framework can calibrate the JMA and KM models and predicts phase transformations during print and heat treatment. Influences of the microstructure composition on thermal and mechanical material behaviors can also be considered in simulations. This is particularly useful, for example, when considering how microstructural features evolve as a function of the number of times that the powder has been recycled. In the case of Ti-6Al-4V, it is known that oxygen uptake during multiple powder uses leads to a loss of ductility after multiple re-uses [14]. In this case, the results of Malinov et al. [15] (an artificial neural network that can generate Ti-6Al-4V TTT diagrams for different oxygen content) could be used in conjunction with the general metallurgical modeling framework to simulate the effect of oxygen concentration on microstructural evolutions and therefore on mechanical properties.

## 4. Demonstration of the framework for two different alloys

The generic framework described above enables users to define metallurgical phase transformations in any metal alloy through a collection

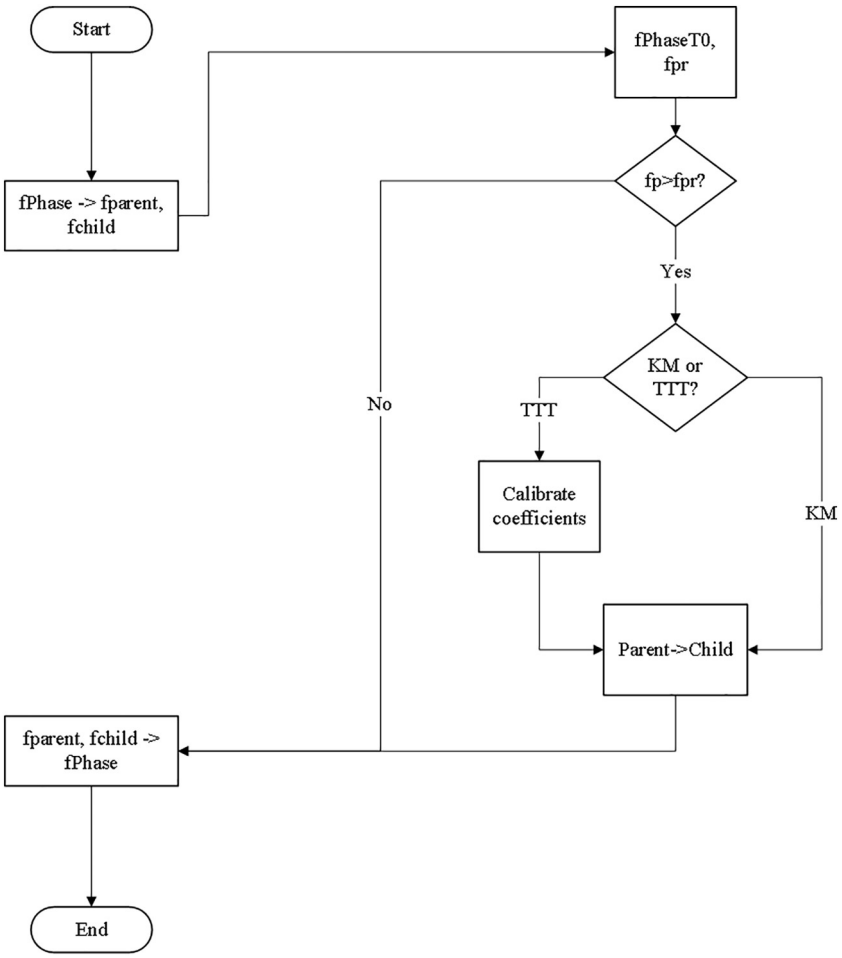


**Fig. 5.** The algorithm to model a martensitic transformation.

of parameter and property tables, and to run finite element simulations of additive manufacturing processes. Two examples are given below with basic validations in one-element tests. It should be noted that although the majority of the metallurgical phase transformations can be described by the JMA/KM equations, some other models are also employed to predict phase transformations, such as a parabolic model. The generic framework allows users to define those transformation models through minimal changes in the user subroutine and input files. Moreover, one may also add features to predict non-generic microstructure morphologies as discussed in the Ti-6Al-4V simulations.

### *4.1. Ti-6Al-4V*

Titanium alloys (Ti-6Al-4V, in particular) are key metals for the aircraft industry because of the combination of excellent mechanical properties with light weight [16]. These properties are very sensitive to the microstructure of the material, and therefore understanding and controlling the microstructure evolution is of great importance in all titanium manufacturing processes [17]. During solidification from the liquid phase, Ti-6Al-4V first solidifies with a body centered cubic (β) crystal structure giving rise to a columnar beta grain structure. During slow cooling from the β phase region, these grains partially transform to the hexagonally close packed (α) phase leaving an equilibrium microstructure containing a mixture of both α and β material. The morphology and distribution of the α phase which forms during this process strongly depend upon the cooling rate and processing conditions; During slow cooling the β transforms to a Widmanstätten microstructure characterized by laths of α. Even slower cooling or annealing close to the beta transus can lead to the formation of a more a equiaxed alpha phase which can form on β grain boundaries. Very high cooling rates, such as those associated with the SLM process, lead to the formation of non-equilibrium metastable martensitic phases the most common of which, α′, has a hexagonal crystal structure similar to α phase but forms by a diffusionless (Martensitic) transformation. α′ has two morphologies an acicular lath morphology similar to Widmanstätten α and massive α′ which differs primarily with respect to the crystallographic orientations of groups of α′ laths. Both α′ morphologies are very often difficult to distinguish from the Widmanstätten α phase. In SLM processes, the high cooling rates leads to the almost complete transformation of the columnar β grains to α′ [18] and subsequent heat treatment, below the β transus temperature, is required to the decomposition the α′ phase into a mixture of the equilibrium α and β phases.

#### *4.1.1. Solid-phase transformation model*

In previous work [1], a phenomenological metallurgical phase transformation model for Ti-6Al-4V alloy was implemented to perform thermal and mechanical analysis of additive manufacturing process. In this paper, the same thermal properties, such as conductivity, latent heat and convection coefficient, are adopted. However, a more comprehensive solid-phase transformation model [17] is implemented to improve the quality of mechanical property predictions. The α′-phase in the previous model is replaced by $\alpha_m$-phase which consists of martensite α and

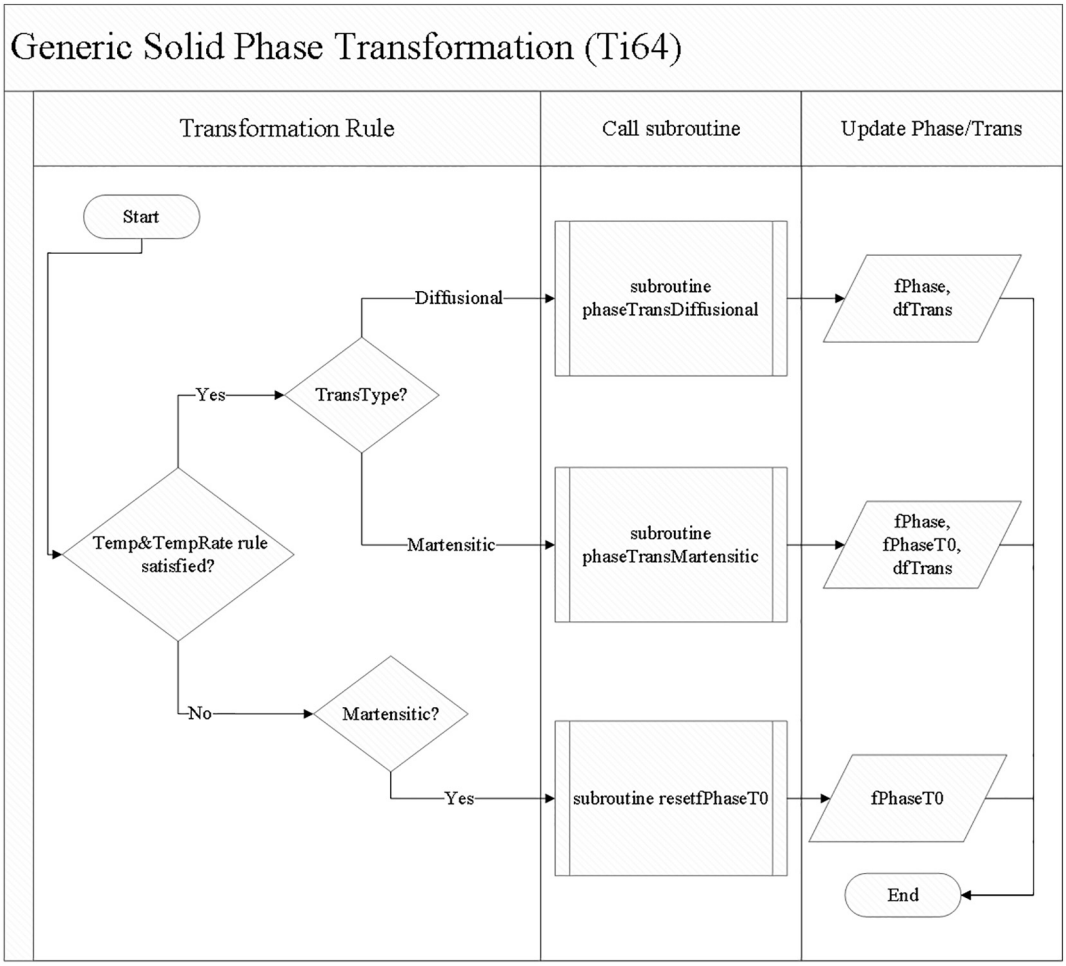


**Fig. 6.** General algorithm to model the generic metallurgical phase transformation framework.

massive α. The previous α-phase is further divided into the equiaxed grain boundary α-phase, $\alpha_{gb}$, and Widmanstätten α-phase, $\alpha_W$ [19].

Five metallurgical phase transformations between the hexagonal close-packed (hcp) $\alpha_{gb}$, $\alpha_W$, $\alpha_m$ and the body-centered cubic (bcc) β-phase are incorporated in the generic parent-children framework. During solidification, the material is considered to be fully β-phase. Due to the subsequent thermal history, one martensitic transformation ($\beta \rightarrow \alpha_m$) and four diffusional transformation ($\beta \rightarrow \alpha_{gb}$, $\beta \rightarrow \alpha_w$, $\alpha_m \rightarrow \beta + \alpha_w$, $\alpha_{gb} + \alpha_w \rightarrow \beta$) are considered for calculation.

The martensitic phase transformation occurs when the cooling rate is larger than 410°C/s and the massive phase transformation occurs when cooling rate is between 20°C/s and 410°C/s. Since the two diffusionless formations have similar chemical compositions and crystal structure, they are assigned one state variable ($f_{\alpha_m}$) in the model [20]. The overall transformation ($\beta \rightarrow \alpha_m$) is described by the KM model, with the transformation start temperature $M_s = 851$°C and $\gamma = 0.005\ ^\circ\mathrm{C}^{-1}$. The $\alpha_m$-phase has an unstable equilibrium crystal structure and can further transform to $\alpha_w$ and β when the sample is annealed at medium high temperature. The transformation ($\alpha_m \rightarrow \beta + \alpha_w$) is described by the JMA model where the coefficients are given in Table 3 [17]. Fraction change of the children phase is proportional to its current equilibrium phase fraction.

At a slower cooling rate from β phase, the alloy forms grain boundary α-phase and Widmanstätten α-phase via diffusion controlled transformations. These transformations ($\beta \rightarrow \alpha_{gb}$, $\beta \rightarrow \alpha_w$) are described by JMA model with two different sets of coefficients n and k. The coefficients are calibrated from the TTT-diagram as shown in Fig. 8 [21]. Although the same JMA model is also applicable for the $\alpha \rightarrow \beta$ transformation, a parabolic growth model [19] is chosen to describe the dissolution of α to β phase ($\alpha_{gb} + \alpha_w \rightarrow \beta$) for the purpose of additive manufacturing process simulation.

$$f_{\alpha_w+\alpha_{gb}}(t+\Delta t) = \begin{cases} 1-f_\beta^{eq}(t+\Delta t) f_{diss}(T)\sqrt{\Delta t + t^*} & 0<\Delta t + t^* < t_{crit}, \\ 1-f_\beta^{eq}(t+\Delta t) = f_{\alpha_w+\alpha_{gb}}^{eq}(t+\Delta t) & \Delta t + t^* > t_{crit}, \end{cases} \tag{8}$$

where $f_{diss}(T) = 2.2 \times 10^{-31} T^{9.89}$ with $T$ in kelvin [21,22], $t_{crit} = (f_{diss}(T))^{-2}$, $t^* = \left(\frac{f_\beta(t)}{f_\beta^{eq}(t+\Delta t) f_{diss}(T)}\right)^2$ and the equilibrium phase fraction $f_\beta^{eq}$ is shown in Fig. 7. It is assumed that $\alpha_w$ transforms to β first and $\alpha_{gb}$ is transformed only when the $\alpha_w$ phase has been extinguished [19].

Two simple one-element tests were performed to validate the metallurgical model. For the first analysis, two heating-cooling cycles with

**Table 3**
JMA coefficients for the transformation ($\alpha' \rightarrow \beta + \alpha_w$).

| Temperature [°C] | $k_1$ [$s^{-n_2}$] | $n_1$ [−] |
|---|---|---|
| 400 | 0.0192 | 0.667 |
| 500 | 0.0147 | 1.106 |
| 700 | 0.0246 | 1.252 |
| 800 | 0.0307 | 1.326 |

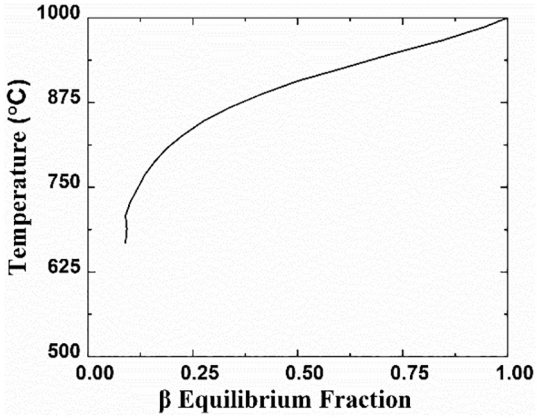


**Fig. 7.** Equilibrium β phase fraction.

different rates between 26°C and 1826°C are assigned. As shown in Fig. 9, the alloy is fully β-phase upon solidification. During rapid cooling, the β-phase transforms to $\alpha_m$ and the diffusional transformations occur slowly upon heating. It is noted that, different from the result in previous model [1], the martensitic and massive phase transformation also occurs at a medium rapid cooling rate (20°C/s to 410°C/s) and the transformation speed is a little slower. For the second analysis, the applied temperature history was extracted from a location in the printing column during the transient heat transfer analysis of an experiment-based column printing model. Printing process and heat treatment are both included, as shown in Fig. 10. In the printing process, the $\alpha_m$-phase is formed during rapid cooling process from the highest temperature. In the subsequent slow cooling process, the diffusional phase transformation occurred is negligible because of extremely low transformation speed at low temperature. As a result, 78% of $\alpha_m$ is predicted at the end of printing. In the heat treating process, $\alpha_m$ transforms to ($\alpha_w$ + $\beta$) through diffusional transformation and the remaining $\beta$ phase from solidification also partially transforms to $\alpha_w$. The phase fraction of $\alpha_w$ is predicted to be 90% at the end of heat treatment.

*4.1.2. Microstructure morphology*

The mechanical properties of Ti-6Al-4V are associated with microstructures and composition of solid phases. The β grain structure is known to play a significant effect on fatigue performance [23], and the Widmanstätten α lath width has been identified to have the largest effect on the strength properties. Therefore, it is important to calculate the α lath width, β grain size and morphology in the FE analysis. These features are added to the metallurgical-microstructural-mechanical model with minimal changes in the generic user subroutine.

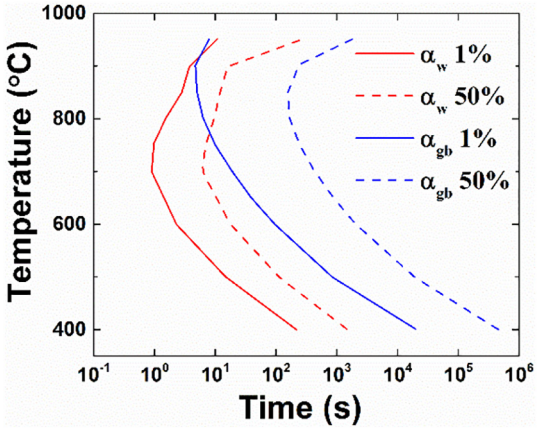


**Fig. 8.** TTT-diagram for diffusional phase transformations $\beta \rightarrow \alpha_{gb}$ *and* $\beta \rightarrow \alpha_w$ in Ti-6Al-4 V.

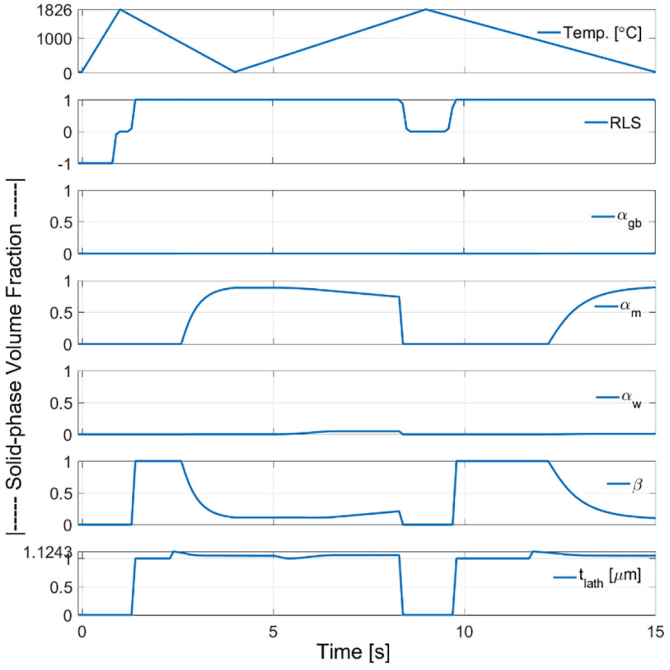


**Fig. 9.** Ti-6Al-4V metallurgical phase transformations and α lath width prediction one element analysis 1.

(a) β grain size and grain morphology

Similar to the previous work, the (solidification) β Grain Size is updated by a parabolic growth law [24] when the temerature is between the β-transus temperature and the solidus temperature.

$$d_{t+\Delta t}^{n} = d_t^n + \Delta t\, k\, \exp\left(-\frac{Q}{R(T-T_Z)}\right) \tag{9}$$

where $d$ is the grain size at time $t$; $d_0 = 0$ is the initial grain size, $n = 2$, $k = 2.2$ m$^2$/s are coefficients, and $Q = 251$ kJ/mol is an activation energy of β-phase of Ti-6Al-4 V; $R = 8.314$ J/(mol · °C) is the universal gas constant.

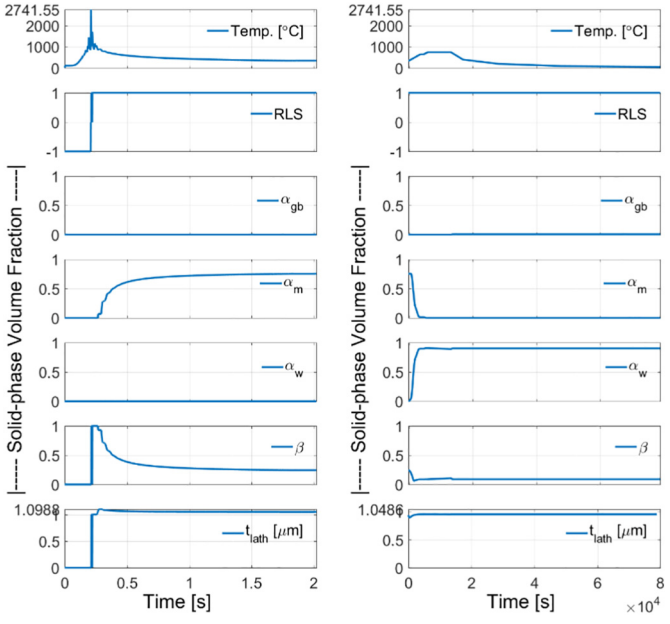


**Fig. 10.** Ti-6Al-4V metallurgical phase transformation one element analysis 2.

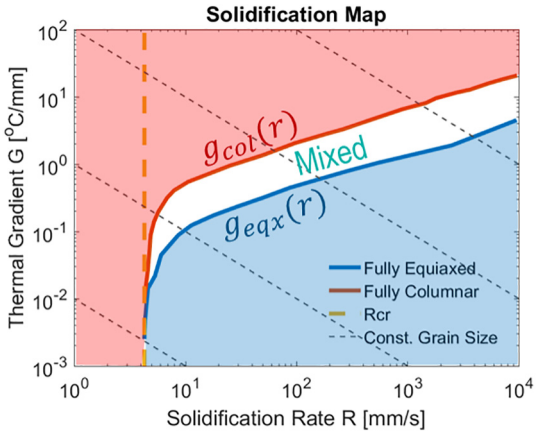


**Fig. 11.** The solidification map for β grain morphology prediction.

The β grain morphology is predicted by an experimentally measured solidification map as shown in Fig. 11 [24]. Given the magnitude of thermal gradient $G$ and solidification rate $R = |\frac{\dot{T}}{G}|$, the $\beta$ morphology can be determined to be equiaxed, columnar or their mixture.

(b) $\alpha$ Lath Width

The Widmanstätten α lath width is assumed to be determined by temperature by an empirical Arrhenius equation as [19],

$$t_{lath}^{eq} = k_{lath} e^{-R_{lath}/T}. \quad (10)$$

And the incremental calculation of the lath size is given as [19], $t_{lath}(t+\Delta t) = (t_{lath} - t_{lath}^{eq}) \times \frac{f_{\alpha_w}(t)}{f_{\alpha_w}(t+\Delta t)} + t_{lath}^{eq}$.

The initial condition $t_{lath}^{0}$ is set to be 1 μm.The parameters are chosen to be Arrhenius prefactor $k_{lath} = 1.42$ μm and activation temperature $R_{lath} = 294$ K [17].

### 4.2. Steel 5140

The generic framework was also applied to a simplified metallurgical model of Steel 5140. Steel 5140 is a low carbon, low alloy chromium, molybdenum, nickel case hardening steel and has good weldability. Thermal properties [25] are given in Tables 4 and 5. Apart from the raw/liquid/solid material states, five metallurgical phases, austenite (A), Bainite (B), Ferrite (F), Pearlite (P) and Martensite (M), were included for calculation. The alloy was considered as fully austenite upon solidification. Eight solid phase transformations between austenite and the other three phases were considered as shown in Table 6.

During cooling, the martensitic transformation (A → M) was described by KM model and the other transformations (A → B, A → F and A → P) were described by JMA model. The transformation temperature bounds and the JMA/KM coefficients were calibrated from the TTT diagram [26] as shown in Fig. 12. During heating, all the phase transformations were modeled by the JMA equation. Since the phase transformations occur very fast [25], coefficients were chosen such that the transformation speeds are ten times of the cooling cases.

**Table 4**
Thermal properties of Steel 5140.

| | Solid | Liquid |
|---|---|---|
| Density[kg/m$^3$] | $7.8 \times 10^3$ | $7.8 \times 10^3$ |
| Conductivity[W/(m · °C)] | 45 | 35 |
| Specific heat capacity[mJ/(ton · °C)] | 650 | 840 |

**Table 5**
Latent heat of Steel 5140.

| | |
|---|---|
| Latent heat of fusion | $2.70 \times 10^5$ J/kg |
| Solidus temperature | 1750°C |
| Liquidus temperature | 1800°C |
| Latent heat of vaporization | $7.60 \times 10^6$ J/kg |
| Liquidus temperature | 2910°C |
| Vaporized temperature | 3010°C |

**Table 6**
Phase transformations considered in the metallurgical model of Steel 5140.

| Transformation | | Type | Occurring conditions |
|---|---|---|---|
| 1 | A → F | Diffusional | $B_s < T < A_1$(Cooling) |
| 2 | A → P | | $B_s < T < A_1$(Cooling) |
| 3 | A → B | | $M_s < T < B_s$(Cooling) |
| 4 | A → M | Martensitic | $M_f < T < M_s$ (Cooling) |
| 5 | F → A | Diffusional | $A_1 < T < A_3$ (Heating) |
| 6 | P → A | | |
| 7 | B → A | | |
| 8 | M → A | | |

One-element validation tests were also conducted. As shown in Fig. 13, the material undergoes heating-cooling cycles with different cooling rates. At slow cooling rate (1 °C/s), the alloy transforms to mainly Ferrite and Pearlite; at medium cooling rate (10 °C/s), a small amount of Bainite phase was predicted; at high cooling rate (100 °C/s), the martensitic phase transformation occurs, and only negligible diffusional formations were predicted. For the purpose of validation test, no quantitative conclusions are drawn here. However, with a more precise metallurgical model (TTT-diagram), the generic subroutine is expected to be applied to the simulation of arbitrary temperature histories in manufacturing process.

## 5. Results and discussions

### 5.1. Experiments and measurements

To support the calibration and validation of the generic metallurgical phase transformation framework, several Ti-6Al-4V SLM samples were manufactured and characterized. For all experimental trials, process parameters, build and recoat times, chamber conditions and powder characteristics were recorded for direct translation into the modeling framework.

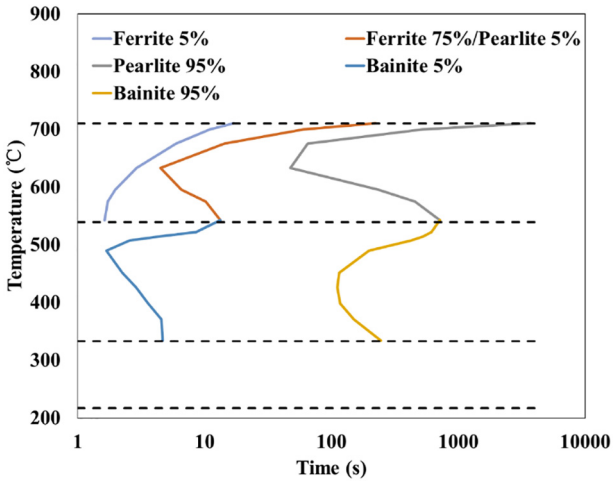


**Fig. 12.** Steel 5140 metallurgical phase transformations TTT-diagram.

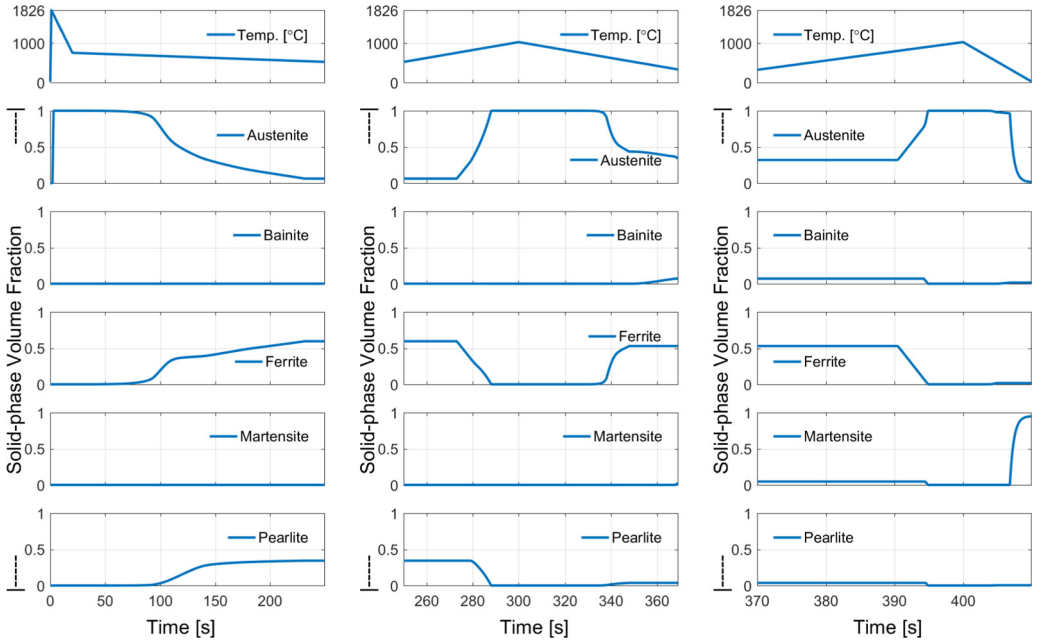


(a) Cooling Rate = 1ºC/s (b) Cooling Rate = 10ºC/s (c) Cooling Rate = 100ºC/s

**Fig. 13.** Steel metallurgical phase transformations.

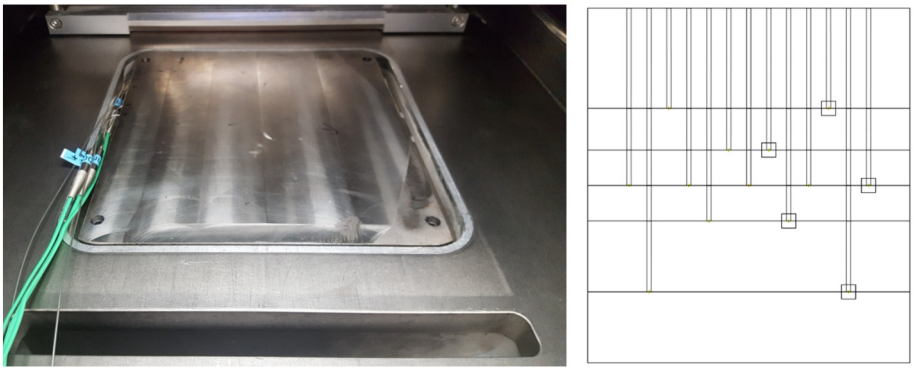

**Fig. 14.** Image of the thermocouple substrate (left) and an illustration (right) showing the location of the blind holes for thermocouple placement.

*5.1.1. Column printing with in situ thermocouple measurements*

Previous work [9] demonstrated the validation of residual stress predictions using the additive manufacturing simulation framework in Abaqus. However, part-level residual stress and distortion predictions can be accurate without capturing the local temperature transients that are required for accurate metallurgical phase transformations modeling. Therefore, a set of tests were defined for the present work whereby local temperature transients could be measured experimentally.

To complement these tests, a bespoke substrate was manufactured by drilling a series of blind holes parallel to the build surface as shown in Fig. 14. The holes were position 0.50 mm below the build surface and Type-K thermocouples were placed at the end of each hole, with the tip of the thermocouple pointing and in contact with the build surface. Five nominally identical cubes with a square cross-section having side length 10 mm and a total build height of 13 mm were built on top of 5 different thermocouples. The cubes were placed sufficiently far from one another to ensure thermal isolation in the thermocouple measurements. A Renishaw AM 250 SLM machine was used with the process parameters shown in Table 7:

During SLM processing of the first 20 layers, the thermocouples recorded temperatures at 100 Hz. The entire cross section (slice) of one square was built before processing of a subsequent cube began. The intention was to have five nominally identical temperature records that

**Table 7**
Process parameters for the thermal validation exercise involving the thermocouple substrate.

| Parameter | Hatch | Border |
|---|---|---|
| Power (W) | 200 | 160 |
| Exposure time (us) | 70 | 30 |
| Point distance (us) | 60 | 20 |
| Hatch spacing (um) | 95 | N/A |
| Beam diameter (um) | 75 | |
| Layer thickness (um) | 60 | |

Notes: Border distance offset of 40um with one boundary contour; powder enters the chamber at room temperature, but the substrate pre-heat temperature was 100 °C. Scan strategy for the in-fill was parallel, alternating scan lines, with an alternation of 67° every layer.

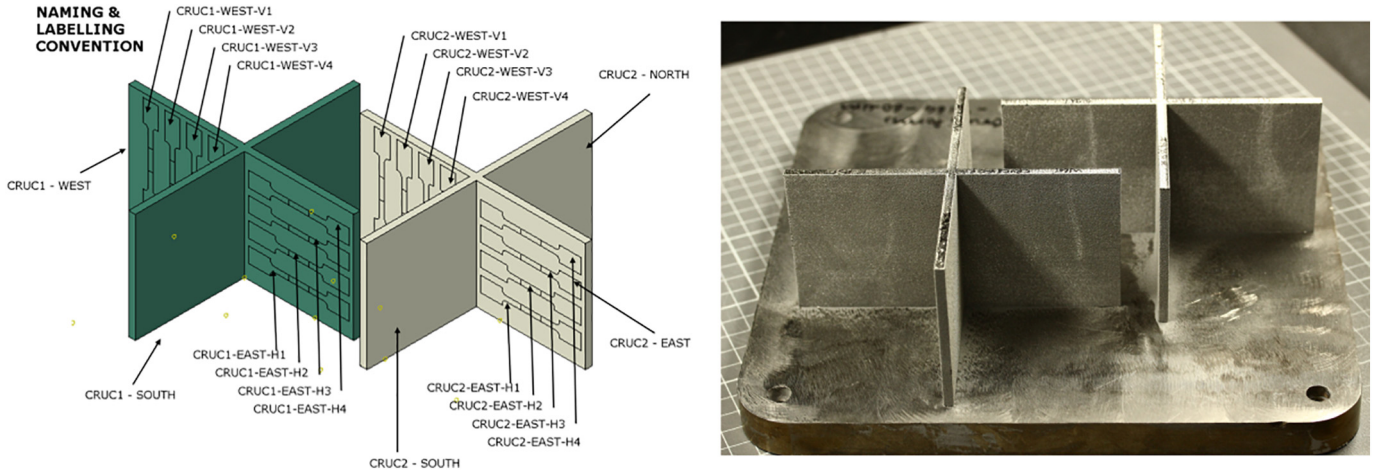


**Fig. 15.** Diagram (left) showing the naming convention for the cruciform specimens and a photograph (right) of the as-built cruciform specimens.

could be aligned using a time shift factor. However, due to the inability to accurately control the placement of the thermocouple tip, coupled with the highly localized temperature transients during SLM processing of the first layers of the build, some differences between measurements could be observed.

*5.1.2. Cruciform printing and tensile testing*

Having validated the heat transfer model using the thermocouple substrate, a new set of experiments was devised to both calibrate and validate the phase transformation model and subsequent structure-property map. Two cruciform specimens were built using the same powder as all previous exercises and the same machine. The cruciform had total build height 40 mm, wall thickness 4 mm, and length 140 mm. The process parameters for the cruciform parts were similar to those of the cubes for the thermal validation except that four boundary contours were used, and the layer-to-layer rotation of scan vectors was 90°.

Following SLM processing of the cruciform specimens, the parts were removed from the substrate. A diagram and photograph of the cruciform parts are shown in Fig. 15.

Of the two cruciform, CRUC1 was left in the as-built condition, and CRUC2 was heat treated. The heat treatment involved using molybdenum heating elements under vacuum ($10^{-5}$ mbar) condition with 10 °C/min heating, holding at 750 °C for 2 h and cooling by convection for 24 h (see Fig. 3). This heat treatment is similar to a typical mill annealing heat treatment applied to wrought products.

The cruciform parts were subjected to metallographic examination. As-deposited and heat-treated specimens were, sectioned, metallographically prepared and examined by back-scatter scanning electron microscopy (SEM) in a Zeiss Sigma SEM. Qualitative chemical area maps were obtained using Oxford Instruments energy-dispersive X-ray (EDX) spectroscopy equipment in the SEM. Additionally, grain structure was quantified using EBSD analysis performed on 115x115μm areas using an accelerating voltage of 30 kV and a step size of 0.05 μm. Analysis was completed using Oxford Instruments Aztec software and grain reconstruction was achieved using a critical misorientation angle of 10° and grain completion to 2°. The average width of laths was determined by dividing the feret length of a grain, by the grain area.

Grain orientation EBSD maps from the as-deposited and heat-treated specimens are shown in Fig. 17. Backscatter SEM images of the two specimens are shown in Fig. 18, which show a, qualitatively, larger lath width

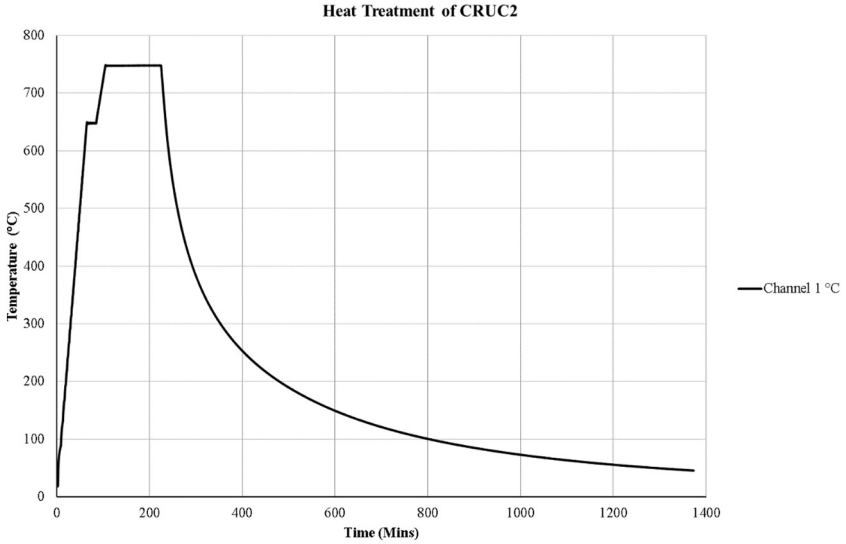


**Fig. 16.** Heat treatment of CRUC2.

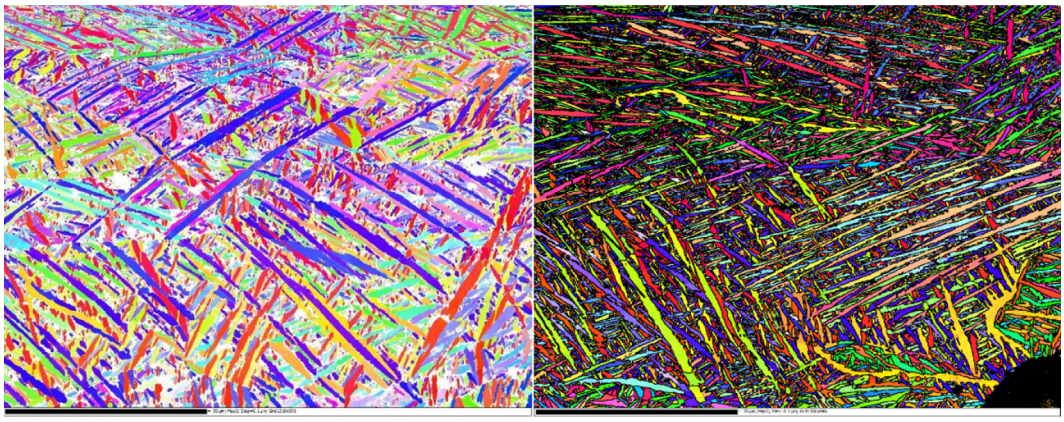

a) As-deposited b) Heat-treated

**Fig. 17.** Grain orientation maps from heat-treated and as-deposited specimens.

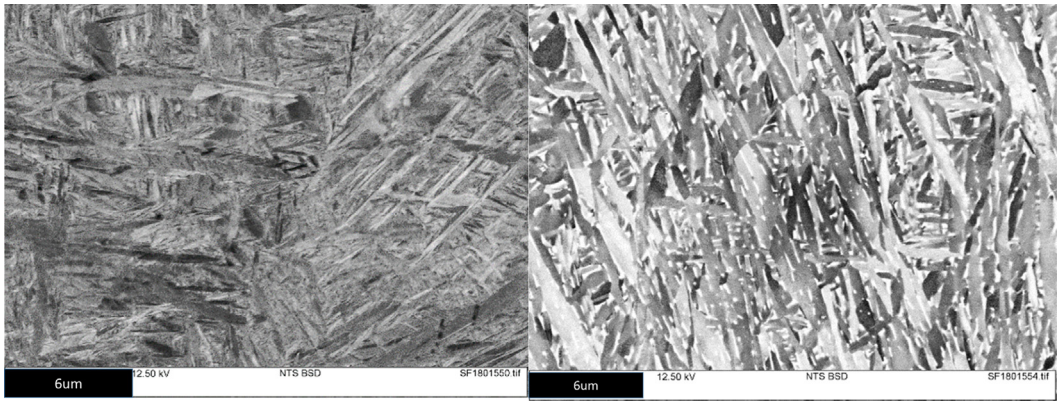


a) As-deposited b) Heat-treated

**Fig. 18.** Back-scatter SEM images of heat-treated and as-deposited specimens.

for the heat-treated specimen. Features showing as white in the backscatter image were evident for the heat-treated specimen, but were absent in the as-deposited specimen. Brighter features, in backscatter images, are indicative of higher atomic number elements being present. EDX elemental mapping was conducted on the heat-treated specimen to determine the chemical makeup of the white features. As can be seen from Fig. 19, the white features were rich in V and deficient in Al.

(a) X-ray diffraction analysis

X-ray diffraction spectra in Bragg-Brentano, i.e. symmetric, configuration was obtained from as deposited and heat-treated specimens, using a Bruker D8 Advance, equipped with a Cu tube X-ray source. Diffraction patterns were obtained between 30 and 130° in 2θ. The purpose of the analysis was to determine differences in the phases present in the

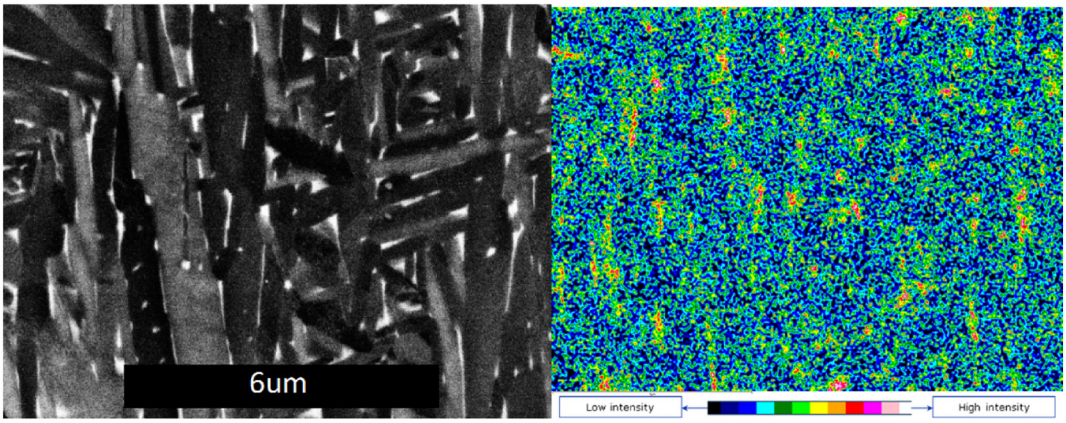


**Fig. 19.** Backscatter SEM images and elemental maps for the heat-treated specimen: Backscatter image (left); V chemical map (right).

as-deposited and heat-treated specimens. Polished metallographic sections, used previously for metallographic analysis, were illuminated with X-rays.

Strain free lattice parameter, $d_0$, measurements, for the α/α′ phases, of the as-deposited and heat-treated specimens, were conducted in order to determine if peak shifts were related to changes in the residual stress state or related to the chemistry of the phases. These features are convoluted when using Bragg-Brentano geometry. The strain-free lattice parameter can be determined from data generated in a standard $\sin^2\psi$ surface residual stress measurement. Such a measurement involves the determination of the d-spacing for a particular diffraction peak at various tilt angles, ψ. A plot of d-spacing vs. $\sin^2\psi$ should be linear with a gradient proportional to the residual stress, σ, i.e.:

$$\frac{\partial d_\psi}{\partial \sin^2\psi} = {}^1/_2 S_2^{hkl}\sigma d_0 \tag{11}$$

$d_0$, can then be determined by interpolation of the d-spacing vs. $\sin^2\psi$ plot to the strain free direction of the biaxial stress state:

$$\psi_{hkl}^{*} = \sin^{-1}\sqrt{\frac{-2S_1^{hkl}}{{}^1/_2 S_2^{hkl}}} \tag{12}$$

The diffraction elastic constants $S_1^{hkl}$ and ${}^1/_2 S_2^{hkl}$ were inferred from single crystal elastic constants for titanium using the Kroner model in the IsoDEC software package. d0 measurements were also obtained by illuminating a polished metallographic specimen with X-rays. It is important to note that although such sectioning of the component would alter the residual stress state, the strain-free lattice parameter would of course be unaffected. The remaining residual stress as well as d0 were determined from examination of the $11\bar{2}4$.

XRD patterns in Bragg-Brentano configuration are shown in Fig. 20. Small β titanium peaks were evident in the heat-treated specimen, but were absent in the as-deposited. Additionally, there was a peak shift to lower 2θ values after heat treatment, as well as a narrowing of the α titanium peaks.

EBSD results indicated changes in lath width with heat treatment. This suggestion is reinforced by the backscatter images which showed an increased grain size for the heat-treated specimen; however, it is challenging to quantify this for the present work as the indexing rate was quite low (70%) in the as-deposited specimen and therefore the statistics were skewed when comparing as-built to heat-treated measurements.

The β titanium phase was not detected, in either of the specimens, through EBSD analysis. However, features with high levels of β stabilizing elements, i.e. V, and lower than back-ground levels of α stabilizing elements, i.e. Al, were detected through backscatter imaging and qualitative chemical analysis. The presence of β titanium was also confirmed by XRD analysis.

The sin2ψ measurements suggested that α′ had decomposed to α + β during heat treatment. After heat treatment, the α lattice parameters were much closer to what would be expected of Ti-6Al-4V.

Peak narrowing was also evident for the heat-treated specimen. Such peak narrowing is indicative of a reduction in deformation, i.e. type III residual stress, and/or an increase in grain size. It is likely that both of these factors would have played a role in the peak narrowing evident in the heat-treated specimen.

### 5.2. Numerical calibration and validation

#### 5.2.1. Column printing and comparison with thermocouple data

The Ti-6Al-4V column printing experiment was modeled with the generic framework using Abaqus/Standard. Fig. 21 shows the finite element model used in the simulations. Twenty layers (60 μm per layer) of five 10 mm × 10 mm cubes were printed on a 226 mm × 248 mm × 15 mm substrate. A uniform fine mesh of 100 μm × 100 μm × 60 μm was used for one cube (referred as cube 5) as highlighted in Fig. 21, and a coarse mesh of 1 mm × 1 mm × 1 mm was used for the other cubes (referred as cube 1–4). The substrate was also partitioned into a coarse mesh (10 mm × 10 mm × 10 mm) part and a fine mesh part underneath cube 5 to perform the analysis.

The laser beam profile was described by the Goldak model with laser spot radius $r = 50$ μm and penetration depth $h = 60$ μm. The laser power absorption coefficient was 55%. Ambient temperature was

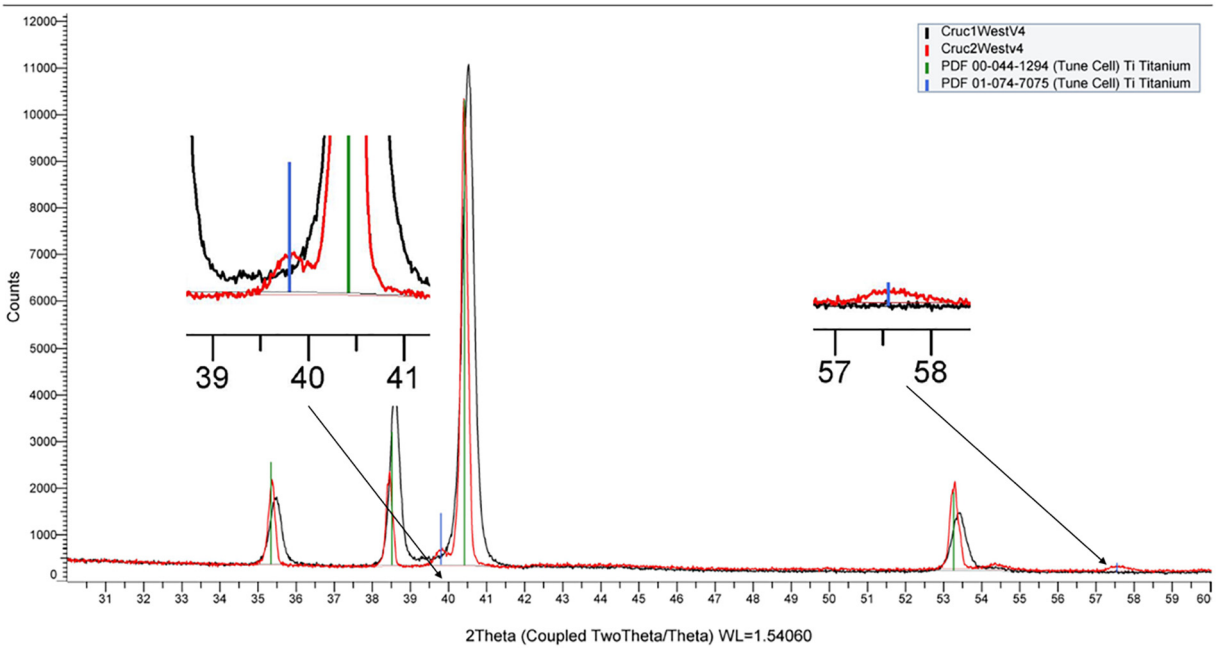


**Fig. 20.** XRD patterns obtained in Bragg-Brentano configuration for as-deposited and heat-treated specimens. Black: as-deposited, Red: heat-treated. (For interpretation of the references to colour in this figure legend, the reader is referred to the web version of this article.)

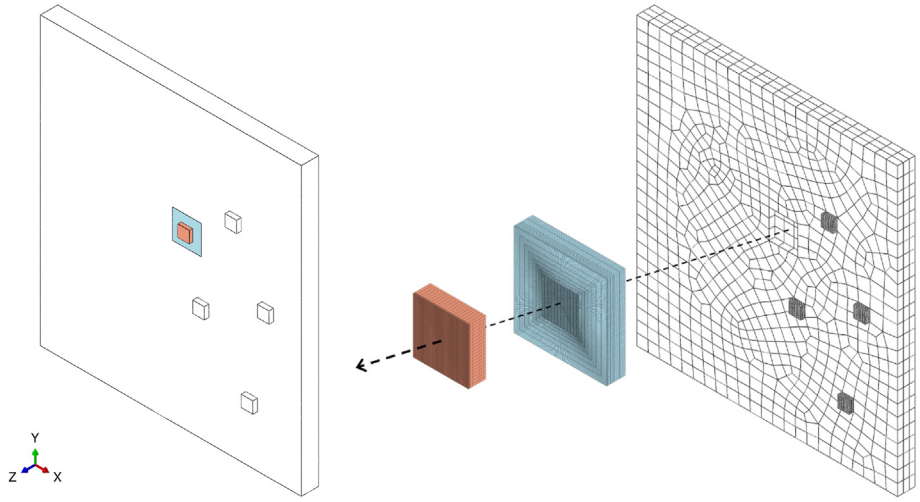


**Fig. 21.** FE model of column printing experiments. Column 5 along with the substrate underneath it is modeled with fine mesh as shown on the right subfigure.

taken to be 26°C and the bottom surface of the substrate was kept at 100 °C during the heat transfer analysis. The time increment was selected to be 0.4 s. Fig. 22 shows the temperature histories at positions with several different depths underneath the cube 5 during first 20 layers printing. Although there are some differences between the finite element predictions of temperature transients and the thermocouple measurements, the overall agreement with regards to the decay of peak temperatures and heating rates are satisfactory. For clarity, the thermocouple measurements provided in Fig. 22 are for the column illustrated in Fig. 21. The thermocouple was located, as described in Section 4.1.1, in a hole drilled into the substrate 0.5 mm below the build surface. The thermocouple is not therefore exposed to the powder layer, but interrogates the local thermal transients from a subsurface measurement. The differences in cooling rates are challenging to address due to the experimental errors incurred with respect to uncertainty in thermocouple placement, the quality of the bond between the thermocouple and the walls which the narrow long holes the thermocouples were placed in. Nevertheless, based on this comparison and previous work comparing thermal measurements with numerical prediction using the same framework [1,27] exercise demonstrates the validation of the heat transfer model.

*5.2.2. Melt Pool predictions: power and scan speed correlations*

Kusuma [29] conducted a series of experiments to study the melt pool characteristics of Ti-6Al-4 V during SLM process and the effect of laser power on melt pool geometry. To validate the local heat transfer analysis of the present additive manufacturing framework, the SLM process of one Ti-6Al-4 V cube was simulated. The computed temperature

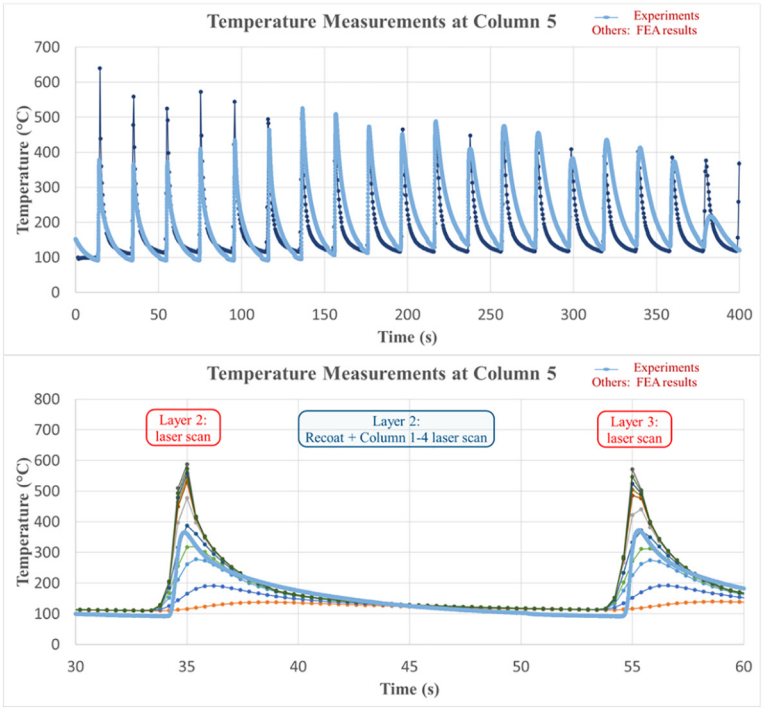


| FEA TCs Depth (mm) |
|---|
| 0 |
| 0.0625 |
| 0.125 |
| 0.1875 |
| 0.25 |
| 0.5 |
| 1.0 |
| 1.5 |
| 2.0 |
| 3.5 |
| 5.0 |

**Fig. 22.** Column printing, temperature experiment measurements vs. FEA predictions at thermo-couple under cube 5. a) first 20 layers printing, the simulation data was taken from the node 0.0625 mm below the cube; b) printing of the second layer. Blue solid line shows the thermocouple recorded temperatures, and all other lines represent finite element predictions at different depths beneath the cube, as shown in the table. The closer the position is to the cube, the higher the temperature is predicted. (For interpretation of the references to colour in this figure legend, the reader is referred to the web version of this article.)

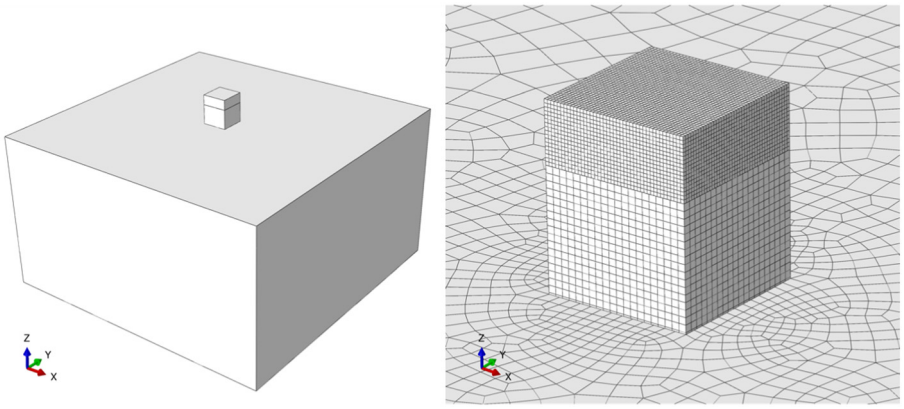

**Fig. 23.** Geometry (left) and mesh (right) of the finite element model for melt pool prediction.

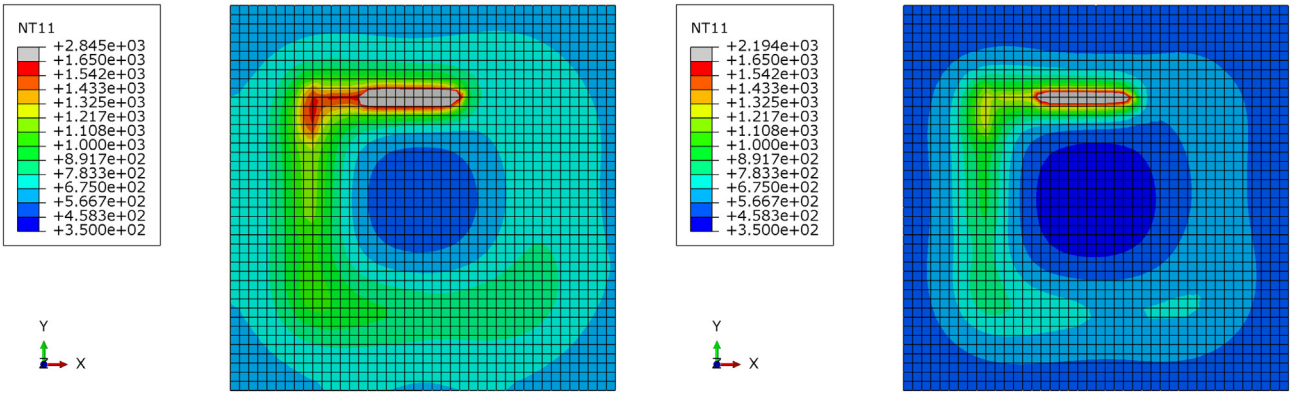


**Fig. 24.** Temperature field at a selected instant during the printing of layer 33: Case 1 (left) and Case 2 (right).

field history was analyzed to obtain melt pool predictions for the process, and further compared with experimental results (Kusuma, 2016). The material's temperature dependent properties used are shown in Fig. 1. Fig. 23 shows the finite element model used in the following simulations, where the cube (2.5 × 2.5 × 3.03 mm) is manufactured on a substrate (30 × 30 × 16.6 mm) made of solid Ti-6Al-4 V. The bottom of the substrate is subject to a temperature boundary condition of 150 °C.

With a layer thickness of 60 μm, a coarse mesh with element size of 125 × 125 × 116 μm was used for the layers numbered 0 to 32, and a fine mesh with element size of 60 × 60 × 60 μm was used for layers 33 to 50. The laser scan path consists of contours only with 80 μm spacing, and a constant scan speed of 600 mm/s was used to generate the time history of the path. Between consecutive layers, a fine recoating step (0.2 s with 0.001 s increments) followed by a coarse recoating step (30 s with 1 s increments) allows the printed layers to cool down and the next layer to be activated. The final melt pool predictions (temperature field) were obtained from layer 33 and 34. The manufacturing process was simulated with laser penetration depth of 50 μm, laser spot radius of 65 μm, and different laser powers of 170 W (Case 1) and 120 W (Case 2). Fig. 24 shows the temperature contour plots from these two cases at a selected instant. As the material has a melting temperature of 1650 °C, areas in the contour plots with temperature higher than this value can be considered as part of the melt pool (grey areas in Fig. 24).

The widths of the melt pool estimated from the contour plots are 120 μm (Case 1) and 90 μm (Case 2). Fig. 25 shows the temperature contour plots in the height direction of the cube at another instant. The depths of the melt pool estimated from the contour plots are 80 μm

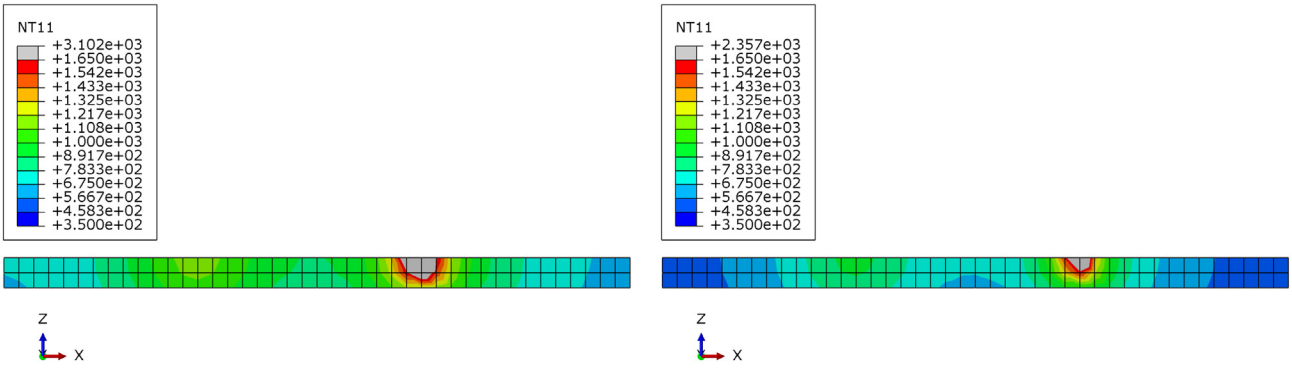


**Fig. 25.** Temperature field at a selected instant during the printing of layer 34: Case 1 (left) and Case 2 (right).

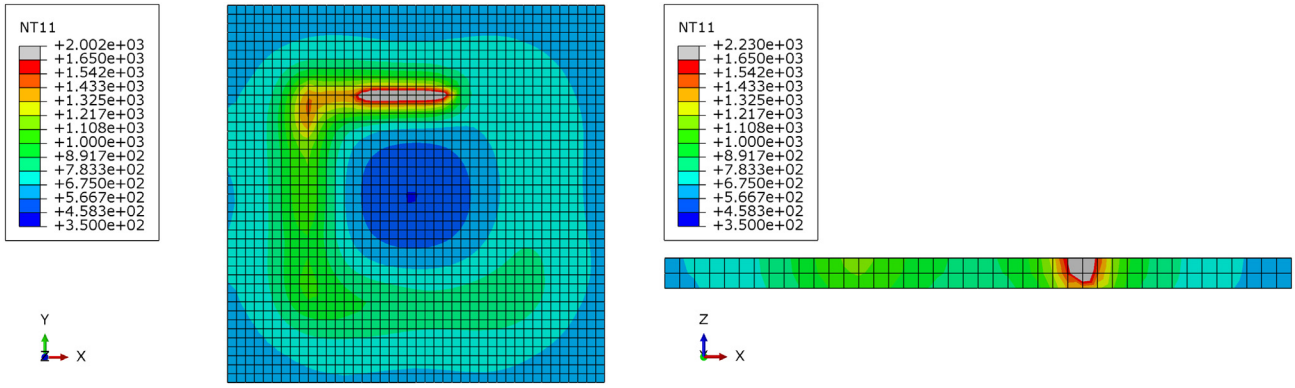


**Fig. 26.** Melt pool width (left) and depth (right) predictions for Case 3.

(Case 1) and 60 μm (Case 2). It can be observed that higher laser power results in a larger melt pool both in width and depth, which agrees with the observation made in experiments (Kusuma, 2016).

The effect of laser penetration depth was studied as Case 3, where the penetration depth is set to 150 μm, and other parameters are the same as in Case 1. Fig. 26 shows the contour plots of Case 3 at the same instant as in Fig. 24 for melt pool width prediction, and in Fig. 25 for melt pool depth prediction. In this case, the melt pool width is estimated to be 80 μm, which is noticeably smaller than that from Case 1. Meanwhile, the depth of the melt pool is increased to about 90 μm, signifying that the same amount of energy is distributed more in the depth direction, and less in the in-plane directions. This observation also validates that, by adjusting the simplified machine information in the presented additive manufacturing framework, the same effects of the real physical machine can be simulated.

*5.2.3. Prediction and validation of lack of fusion*

Ali et al. [28] conducted a series of experiments to study the quality of SLM manufactured Ti-6Al-4 V with respect to different power and exposure time as shown in Fig. 27, where the black voids represent unfused powder in the manufactured layer. Similar results can also be predicted by the present metallurgical phase transformation framework. Fig. 28 shows the raw/solid/liquid (RLS) states in layer 34 for Case 1 and Case 2, which corresponds to exposure time of 60 μs (the first column in Fig. 16). Distributed unfused powder (blue areas on the contour plots) can be observed when using laser power of 120 W, while almost the entire layer is fused using laser power of 170 W. The prediction agrees with the trend shown in experiments, which means the effect of laser power on the states of powder can be captured by the present framework.

*5.2.4. Cruciform printing, dog bone samples*

Following the experiments presented in Section 5.1.2, the SLM processing of the cruciform specimens and the tensile tests on one dog bone sample were simulated within the additive manufacturing framework in Abaqus/Standard. Fig. 29 shows the geometry and mesh of the finite element model for the heat transfer analysis. To simplify the manufacturing process, only the reduced section of the CRUC1-EAST-H1 dog bone specimen (shown in Fig. 15) was modeled with a fine mesh (60 × 58.8 × 60 μm elements). The layers below this section and

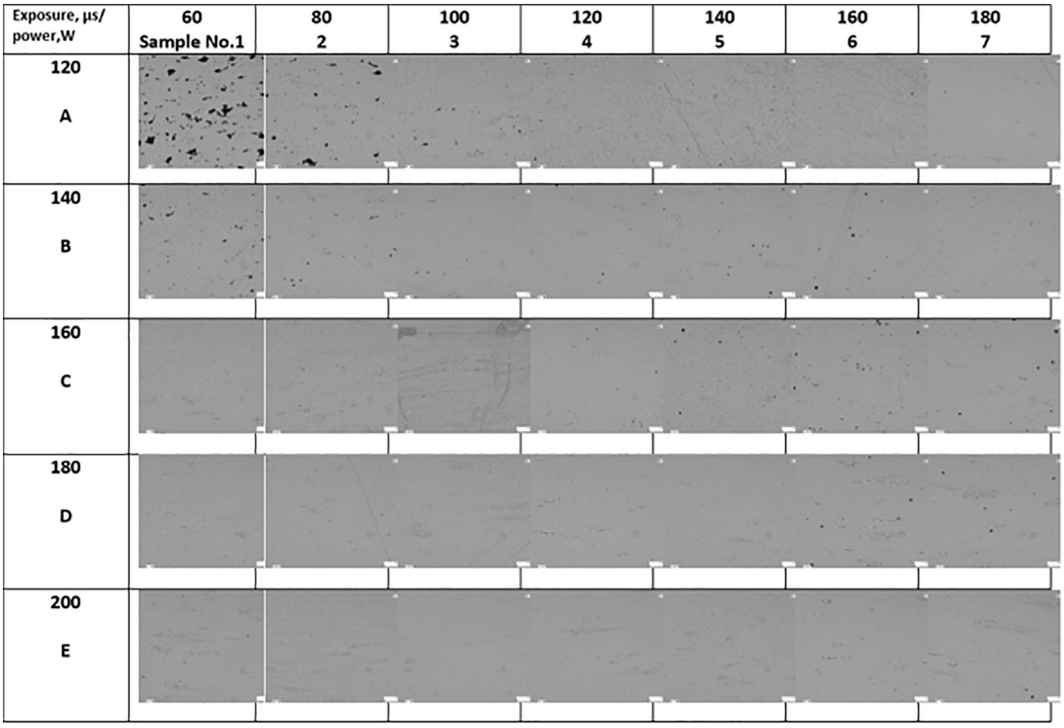


**Fig. 27.** Fused powder density for different power and exposure [28].

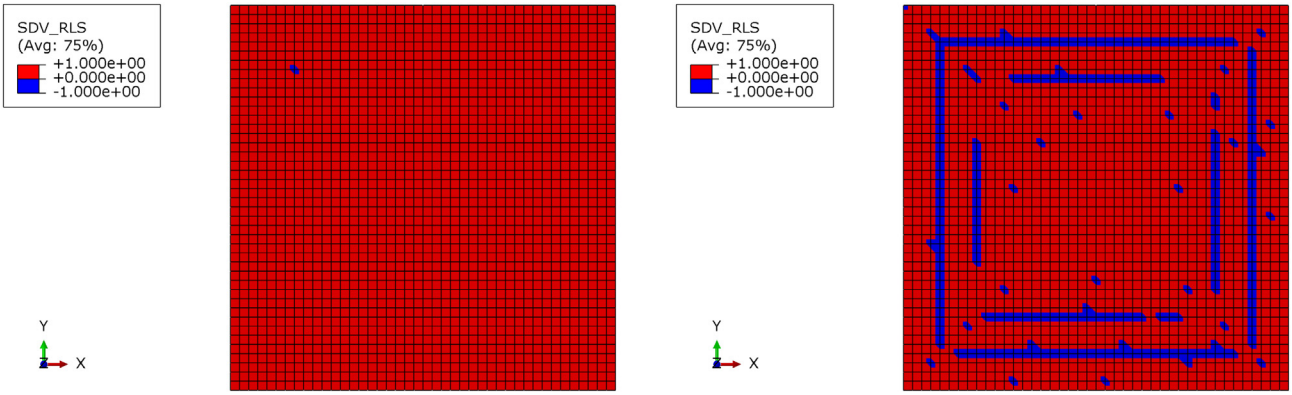


**Fig. 28.** RLS states contour plots for layer 34: Case 1 (left) and Case 2 (right).

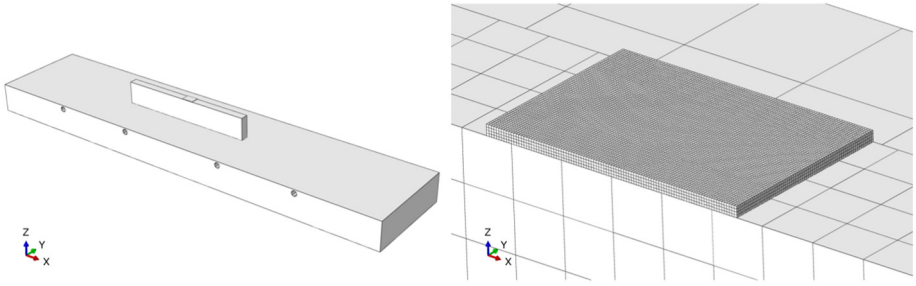

**Fig. 29.** Geometry (left) and mesh (right) of the SLM process on one dog bone specimen in the cruciform model.

above the substrate are modeled with a coarse mesh of element size 1.2 × 1 × 1.15 mm. The overall size of the finely computed section is 6 × 4 × 0.24 mm, which corresponds to four layers of laser melting using the machine information from Case 1 of Section 5.2.2. The same laser scan paths as in the experiments were generated for the simulation, where each layer contains 4 boundary contours, and hatch-type infill with 90° alternation angle between layers. Recoating steps following those from Case 1 of Section 5.2.2 were used between consecutive layers.

A snapshot of a temperature evolutions during the printing of the gage length section of the dog bone specimen is shown in Fig. 30.

Phase fraction volumes are predicted at each integration point as driven by the rapidly evolving temperatures. While contour plots of the phases at various stages during print are available, no clear trend was able to be identified and therefore presenting such contour plots would not be useful. Similar to what was observed experimentally, a mixture of existing phases exist at all locations without a clear trend on how these might evolve locally within the sample. Volume fractions were then averaged for the entire specimen to compute an average volume fraction at the end of the print and at the end of the heat treatment history, as shown in Table 8.

## 6. Conclusions

While recent progress in improving the understanding of additive manufacturing processes, the process is often hindered by variable strength parts with inferior fatigue life when compared to traditional manufacturing processes such as forging and casting. The complex multiscale-multiphysics aspects of metallurgical phase transformations

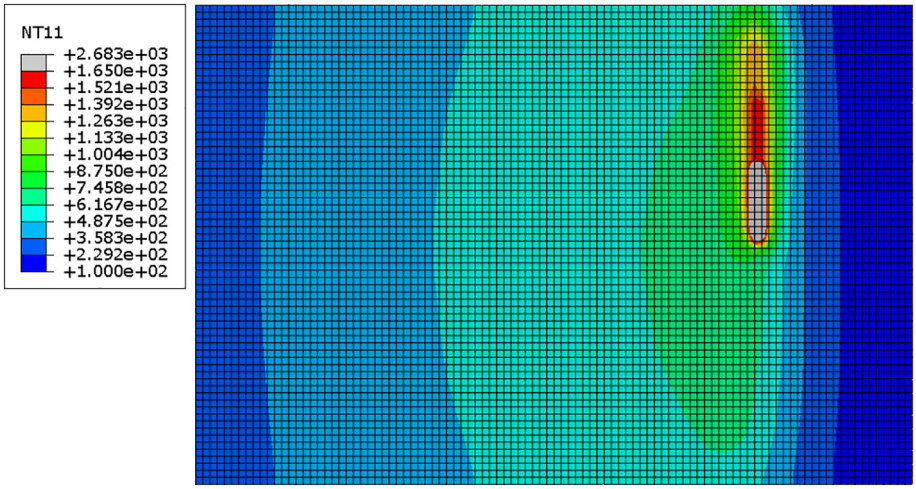


**Fig. 30.** Temperature evolutions: snapshot during a lasering sequence. Grey contour plots represent temperature as above melting.

**Table 8**
Volume fraction predictions.

| | $\beta$ | $\alpha'$ | $\alpha$ |
|---|---|---|---|
| As-built (simulation) | 0.2% | 95.58% | 4.212% |
| As-built (experimental) | None observed | 93.87% | 6.13% (by morphology) |
| After heat treatment (simulation) | 11.8% | 0.1% | 88.04% |
| After heat treatment (experimental) | 4.3% | Cannot distinguish between two (95.7%) | |

are at the very center of this problem. In this paper we have introduced a general framework for predicting volume fractions of metallurgical phase transformations as an add-on to a previously introduced general FE-based framework for predicting temperature evolutions, distortions, and residual stresses in printed parts. The modeling framework was demonstrated for two different alloys, Ti-6Al-4V and Steel 5140:

1. Computes detailed temperature evolutions and gradients associated with rapid heating and cooling
2. Requires as input the collection of all relevant metallurgical phase transformations that can take place, diffusional or non-diffusional.
3. Can be calibrated upfront or on-the-fly from temperature transformation diagrams
4. Predicts volume fractions of phases post printing or post heat treatment.

Numerical models have little value unless they provide reasonable predictions when compared to physical test measurements. Temperature measurements and volume fractions metallographic assessments via EBSD/XRD techniques of printed and heat-treated samples were performed. Numerical predictions were compared against test measurement with reasonable success.

The combined numerical and experimental methodology introduced in this paper provides a possible pragmatic approach to address process-structure-property-performance relationships in additive manufacturing. Whilst the proposed approach is not derived entirely from first principles (like emerging integrated computational materials engineering approaches), the approach is valuable in that it seems it can be reasonably calibrated with a reasonable number of experimental trials. Once the model is calibrated, the end user has access to a collection of metallurgical modeling tools that could eventually help inform process parameter optimization in reasonable computational run times. Therefore, whilst still a continuum-level internal state variable approach, the method can directly link processing conditions to microstructural features which can be explored and optimized iteratively. Future work will investigate the influence of microstructure features on mechanical performance to address the process-structure-property-performance relationship in additive manufacturing.

## Data availability

The raw and processed data required to reproduce some of these findings are available to download from the Mendeley Data for Journals.

## CRediT authorship contribution statement

**Qi Zhang:** Methodology, Software, Validation. **Jiawen Xie:** Methodology, Software, Investigation. **Zhenyuan Gao:** Validation, Formal analysis. **Tyler London:** Methodology, Resources, Data curation. **David Griffiths:** Formal analysis, Resources. **Victor Oancea:** Conceptualization, Resources, Data curation.

## References

[1] J. Xie, V. Oancea, J. Hurtado, Phase Transformations in Metals During Additive Manufacturing Processes, 2017, NAFEMS World Congress, 2017.
[2] M.M. Kirka, P. Nandwana, Y. Lee, R.R. Dehoff, Solidification and solid-state transformation sciences in metals additive manufacturing, Scr. Mater. 135 (2017) 130–134.
[3] M.J. Anderson, C. Panwisawas, Y. Sovani, R.P. Turner, J.W. Brooks, H.C. Basoalto, Mean-field modelling of the intermetallic precipitate phases during heat treatment and additive manufacture of Inconel 718, Acta Mater. 156 (2018) 432–445.
[4] Abaqus, User's manual, https://www.3ds.com/products-services/simulia/support/documentation/ 2018.
[5] J. Goldak, A. Chakravarti, M. Bibby, A new finite element model for welding heat sources, Metall. Trans. B 15 (2) (1984) 299–305.
[6] Z. Fan, F. Liou, Numerical modeling of the additive manufacturing (AM) processes of titanium alloy, Titanium Alloys-towards Achieving Enhanced Properties for Diversified Applications, InTech, 2012.
[7] W. King, A.T. Anderson, R.M. Ferencz, N.E. Hodge, C. Kamath, S.A. Khairallah, Overview of modelling and simulation of metal powder bed fusion process at Lawrence Livermore National Laboratory, Mater. Sci. Technol. 31 (8) (2015) 957–968.
[8] D. Pal, N. Patil, K. Zeng, B. Stucker, An integrated approach to additive manufacturing simulations using physics based, coupled multiscale process modeling, J. Manuf. Sci. Eng. 136 (6) (2014) 061022.
[9] S. Tripathy, C. Chin, T. London, U. Ankalkhope, V. Oancea, Process Modeling and Validation of Powder Bed Metal Additive Manufacturing, 2017, NAFEMS World Congress, 2017.
[10] A. Crespo, Modelling of heat transfer and phase transformations in the rapid manufacturing of titanium components, Convection and Conduction Heat Transfer, InTech, 2011.
[11] Y.K. Ko, V. Sahai, R.A. Overfelt, J.T. Berry, Prediction of Porosity in Cast Equiaxed Alloy 718 (No. CONF-9509118--), Minerals, Metals and Materials Society, Warrendale, PA (United States), 1995.
[12] P.K. Sung, D.R. Poirier, S.D. Felicelli, E.J. Poirier, A. Ahmed, Simulations of microporosity in IN718 equiaxed investment castings, J. Cryst. Growth 226 (2–3) (2001) 363–377.
[13] H. Zhao, L. He, W.C. Niu, B. Zhang, Investigation on porosity suppression in deep-penetration laser welding by using computational fluid dynamics, J. Laser Appl. 28 (3) (2016) 032011.
[14] H.P. Tang, M. Qian, N. Liu, X.Z. Zhang, G.Y. Yang, J. Wang, Effect of powder reuse times on additive manufacturing of Ti-6Al-4V by selective electron beam melting, JOM 67 (3) (2015) 555–563.
[15] S. Malinov, W. Sha, Z. Guo, Application of artificial neural network for prediction of time–temperature–transformation diagrams in titanium alloys, Mater. Sci. Eng. A 283 (1–2) (2000) 1–10.
[16] C. Leyens, M.eds. Peters, Titanium and Titanium Alloys: Fundamentals and Applications, John Wiley & Sons, 2003.
[17] C.C. Murgau, Microstructure Model for Ti-6Al-4V Used in Simulation of Additive Manufacturing, Doctoral dissertation, Doctoral thesis Luleå University of Technology, 2016.
[18] J. Yang, H. Yu, J. Yin, M. Gao, Z. Wang, X. Zeng, Formation and control of martensite in Ti-6Al-4V alloy produced by selective laser melting, Mater. Des. 108 (2016) 308–318.
[19] C.C. Murgau, R. Pederson, L.E. Lindgren, A model for Ti–6Al–4V microstructure evolution for arbitrary temperature changes, Model. Simul. Mater. Sci. Eng. 20 (5) (2012) 055006.
[20] T. Ahmed, H.J. Rack, Phase transformations during cooling in $\alpha+\beta$ titanium alloys, Mater. Sci. Eng. A 243 (1–2) (1998) 206–211.
[21] S.M. Kelly, Thermal and microstructure modeling of metal deposition processes with application to Ti-6Al-4V, Doctoral dissertation Virginia Tech, 2004.
[22] S.M. Kelly, S.S. Babu, S.A. David, T. Zacharia, S.L. Kampe, A microstructure model for laser processing of Ti-6Al-4V, International Congress on Applications of Lasers & Electro-optics, Vol. 2005, No. 1, LIA October, 2005, p. 1005.
[23] M.J. Donachie, Titanium: A Technical Guide, ASM international, 2000.
[24] P.A. Kobryn, S.L. Semiatin, Microstructure and texture evolution during solidification processing of Ti–6Al–4V, J. Mater. Process. Technol. 135 (2–3) (2003) 330–339.
[25] W. Piekarska, M. Kubiak, A. Bokota, Numerical simulation of thermal phenomena and phase transformations in laser-arc hybrid welded joints, Arch. Metall. Mater. 56 (2) (2011) 409–421.
[26] N. Saunders, Z. Guo, X. Li, A.P. Miodownik, J.P. Schillé, The Calculation of TTT and CCT Diagrams for General Steels, JMatPro Software Literature, 2004.
[27] S. Simunovic, A. Nycz, M. Noakes, C. Chin, V. Oancea, Metal Big Area Additive Manufacturing: Process Modeling and Validation, 2017, NAFEMS World Congress, 2017.
[28] H. Ali, L. Ma, H. Ghadbeigi, K. Mumtaz, In-situ residual stress reduction, martensitic decomposition and mechanical properties enhancement through high temperature powder bed pre-heating of selective laser melted Ti6Al4V, Mater. Sci. Eng. A 695 (2017) 211–220.
[29] C. Kusuma, The effect of laser power and scan speed on melt pool characteristics of pure titanium and Ti-6Al-4V alloy for selective laser melting, 2016.